

1 **StageIV-IRC: A High-resolution Dataset of Extreme Orographic Quantitative**  
2 **Precipitation Estimates (QPE) Constrained to Water Budget Closure for**  
3 **Historical Floods in the Appalachian Mountains**

4 Mochi Liao<sup>1</sup> and Ana P. Barros<sup>1</sup>

5 1. Civil and Environmental Engineering, University of Illinois Urbana-  
6 Champaign, Urbana, IL

7 **Corresponding Author:**

8 Dr. Ana Barros

9 E-mail: [barros@illinois.edu](mailto:barros@illinois.edu)

10 Phone: +1 217-333-8038

11

Field Code Changed

Formatted: Portuguese (Brazil)

12 **Abstract**

13 Quantitative Flood Estimation (QFE) in complex terrain remains a grand challenge in  
14 operational hydrology due to the lack of accurate high-resolution Quantitative Precipitation  
15 Estimates (QPE) for operational forecasting and for calibrating hydrologic models. Here, we  
16 present a high-resolution (i.e., 250m, 5-minute-hourly) QPE dataset for 215 extreme rainfall events  
17 occurred in 26 gauged mountainous basins in the Appalachian Mountains from 2008 to 2024. This  
18 dataset is developed by applying Inverse Rainfall Corrections (IRC) derived from physically-based  
19 rainfall-runoff modeling (Liao and Barros, 2022 and 2023) to the Next Generation Weather Radar  
20 (NEXRAD) Stage IV analysis (4 km resolution, hourly). The corrected Stage IV analysis QPE is  
21 referred to as StageIV-IRC (StageIV with Inverse Rainfall Correction). The unique advantage of  
22 this StageIV-IRC QPE dataset is its agreement with ground-based rainfall measurements while  
23 achieving water budget closure at the storm-flood event scale and minimizing uncertainty from  
24 initial soil moisture conditions ~~by integrating using the~~ Initial Condition Corrections ~~s.~~ ~~-(ICC) in~~  
25 ~~the IRC framework~~ —(Liao and Barros, 2025). This dataset is the first QPE dataset aiming to  
26 improve QFE in complex terrain by reducing biases for extreme precipitation events, and it can be  
27 used to evaluate the skill of hydrologic models in the same basins and support model calibration.  
28 The StageIV-IRC QPE dataset and the companion initial soil moisture maps derived from the ICC  
29 module are publicly available at <https://doi.org/10.5281/zenodo.14028866>.

30

## 31 **1. Introduction**

32 Over the past few decades, extreme precipitation has become an increasingly important  
33 research topic due to its social, economic, and environmental impacts (e.g., Alimonti et al., 2022;  
34 Wernberg et al., 2013). Studies show that both total annual precipitation and extreme precipitation  
35 events have increased in the US and in other parts of the world during the last century (e.g., Milly  
36 et al., 2002), often resulting in floods (e.g., Pielke and Doughton, 2002), and flash floods in the  
37 context of complex terrain due to steep slopes (e.g., Schumacher, 2017; Czigány et al., 2010).  
38 Flash floods are characterized by fast rainfall-runoff responses on the scale of a few hours (< 6  
39 hours) after extreme precipitation events for watershed areas often ranging from a few tens to  
40 hundreds of square kilometers (e.g., Borga et al., 2014; Lumbroso and Gaume, 2012). As one of  
41 the deadliest natural hazards, flash floods are often associated with landslide events (e.g., Tao and  
42 Barros, 2014; Gupta et al., 2016; Deijns et al., 2022) and cause loss of life and property damage  
43 (Špitalar et al., 2014), such as recently in the last three years in the Appalachian Mountains, USA,  
44 and in Southern Spain. Despite extensive studies to improve flash flood simulations in small  
45 headwater basins, hydrological skill scores (e.g., Kling-Gupta Efficiency or KGE) remain poor at  
46 event scales largely due to significant difficulties involved in estimating highly localized  
47 orographic precipitation in complex terrain, which in turn implies that hydrologic models are not  
48 calibrated using forcing representative of realistic extreme events (e.g., Andrieu et al. 1997;  
49 Huffman et al., 2007; Mtibaa and Asano, 2022).

50 Current approaches involved in precipitation measurement and Quantitative Precipitation  
51 Estimation (i.e., QPE) broadly include in-situ point-scale observations using rain gauges and  
52 disdrometers, and remote spatial observations using ground-based radar and space-based sensors.  
53 In complex terrain, there is often a scarcity of in-situ measurements due to difficult access. For

54 example, the rain gauge network from NASA's Integrated Precipitation and Hydrology Experiment  
55 is the only relatively dense rain gauge network installed at high elevations in the entire  
56 Appalachians (e.g., Barros et al. 2014). Other QPE products (e.g., radar QPE data) are plagued by  
57 uncertainties from various sources (e.g., ground clutter artifacts, retrieval uncertainties, and radar  
58 viewing geometry (Villarini and Krajewski, 2010; Arulraj and Barros, 2021; Kreklow et al., 2020;  
59 Huffman et al., 2007; Andrieu et al., 1997; Durden et al., 1998). Numerical weather prediction  
60 (NWP) is an alternative to measurement. However, QPE products from NWP models are  
61 characterized by significant uncertainties when evaluated against rain gauges (e.g., Zhang and  
62 Anagnostou, 2019), leading to large flood simulation errors when used as inputs to hydrological  
63 models, or introducing large structural uncertainty when used for model calibration (e.g., Tao et  
64 al., 2016; Weiland et al., 2015; Diomede et al., 2008; Kobold and Suselj, 2005). Due to these  
65 uncertainties and errors involved, focus has been directed towards enhancing QPE using various  
66 methods: data merging of raingauge and radar precipitation (e.g., McKee and Binns, 2016;  
67 Goudenhoofdt and Delobbe, 2009; Delrieu et al., 2014; Nanding et al., 2015; Sideris et al. 2013;  
68 Schiemann et al. 2011), combined radar reflectivity and retrieval corrections (e.g., Vignal et al.,  
69 2000; Shao et al., 2021; Dinku et al., 2002), and data assimilation into NWP models (e.g.,  
70 Rafiecinasab et al., 2015; Wehbe et al., 2020). Rain gauge and disdrometer measurements are often  
71 used as references for these QPE optimization approaches (e.g., Harrison et al., 2000; Shao et al.,  
72 2021; Fulton et al., 1998). The 'ground truth', however, has its own error (e.g., spatial  
73 representativeness, wind artifacts around the gauge orifice, and calibration, among others;  
74 Kochendorfer et al., 2017), and fails to capture highly localized orographic enhancement (e.g., Prat  
75 and Barros, 2010b; Gentilucci et al., 2021; Buytaert et al., 2006). Gauge-radar fusion often relies  
76 on geostatistical assumptions that are primarily distance-based (e.g., Areerachakul et al., 2022;

77 Cassiraga et al., 2021; Wang et al., 2020; Maggioni and Massari, 2018), lacking the full picture of  
78 complex basin topography, which has a regulating role in orographic precipitation processes.

79 To address this long-standing QPE challenge in complex terrain, a general QPE error  
80 quantification framework was developed leveraging widely available quality United States  
81 Geological Survey (USGS) streamflow observations at the outlet of headwater basins in complex  
82 terrain, consisting of 2 distinct paths: 1) rain gauge bias correction, and 2) grid-level QPE  
83 correction constrained to watershed-scale water budget closure. The first pathway includes rain  
84 gauge bias corrections at gauge locations both at the diurnal and climate scales, and the  
85 geostatistical distribution of rain gauge biases across a basin. The second pathway includes an  
86 innovative inverse QPE correction method by backward propagating runoff uncertainty using a  
87 hydrological model via streamlines to precipitation at storm-event scale, and the methodology is  
88 termed Inverse Rainfall Correction (IRC), which is developed by the same authors (Liao and  
89 Barros, 2022 or LB22).

90 LB22 found that initial soil moisture uncertainty causes inferior performance of IRC  
91 because large initial condition errors lead to significant uncertainties in travel time distributions.  
92 Soil moisture is considered a particularly important factor among soil properties due to its  
93 significant role in affecting the generation of runoff, hence dramatically altering the timing of flood  
94 front and its magnitudes (e.g., Vivoni et al., 2007; Marchi et al., 2010; Penna et al., 2011), and soil  
95 moisture can vary dramatically at hourly timescales, changing from fully saturation levels to  
96 wilting point levels conditional on the specific texture and other properties of the soils (Grillakis  
97 et al., 2016). Initial soil moisture conditions can therefore determine whether a rainstorm produces  
98 a major flash flood or not (e.g., Komma et al., 2007; Zehe and Blöschl, 2004). However, due to  
99 the limited availability of soil moisture sensors, there are not many studies quantifying the impact

100 of soil moisture on runoff simulation (e.g., Silvestro et al., 2019; Laiolo et al., 2016; Zappa et al.,  
101 2011; Uber et al., 2018). Liao and Barros (2025b) developed an Initial Condition Correction (ICC),  
102 which is based on travel time distributions and is coupled with the general IRC approach,  
103 demonstrating large improvements in initial soil moisture estimation. Note that when  
104 implementing the IRC and ICC, we are using a fully distributed physics-based uncalibrated model  
105 (i.e. Duke Coupled Hydrological Model, DCHM) that has been used successfully for more than  
106 two decades for hydrologic studies in the Southern and Central Appalachians (e.g., Tao and Barros,  
107 2013, 2014, 2018 and 2019; Tao et al. 2016; Yildiz and Barros 2004, 2007 and 2009), and  
108 consequently uncertainty from model structure and model parameters is assumed to be small.  
109 Hydrological model parameters certainly have an impact on rainfall-runoff response, but they are  
110 generally only of secondary importance compared to the precipitation proper and antecedent soil  
111 moisture distributions, especially for smaller basins (e.g., Dobler et al., 2012; Mockler et al., 2016).

112 In this work, IRC and ICC are combined into one structure (referred to as the IRC-ICC  
113 framework) to construct an improved QPE dataset aiming to close the water budget at the scale of  
114 storm-flood events along the entire Appalachian Mountains (e.g., Liao and Barros 2022 and  
115 2025b). The study region is set to be the Appalachian Mountains because they are prone to extreme  
116 precipitation and flash floods due to orographic lift of moisture-laden air masses coming from the  
117 Gulf of Mexico and the Atlantic Ocean (e.g., Troch et al., 1994; Smith et al., 2011; Liao and  
118 Barros, 2023). A recent example is Hurricane Helene, which caused over 200 deaths and over \$50  
119 billion in property damage in the Southeast US in September 2024. The IRC-ICC framework is  
120 employed in 26 headwater basins and 215 extreme events (during 2008-2024) using the Next  
121 Generation Weather Radar (NEXRAD) StageIV dataset as original inputs, at a spatial and temporal

122 resolution of 250 m and 5 minutes, respectively, and the improved post IRC-ICC QPE data (i.e.,  
123 StageIV-IRC) are made available in this study.

124 The manuscript is organized as follows. The data sources and the QPE error quantification  
125 framework, which consists of rain gauge bias correction and the IRC-ICC framework, are detailed  
126 in Section 2. Section 3 presents this new dataset (StageIV-IRC) along with data assessment from  
127 various aspects. Section 4 discusses the potential application of this new dataset and future work.  
128 Section 5 provides access to the dataset and a summary of the work.

129

## 130 **2. Data and Methodology**

### 131 **2.1 Radar QPE StageIV**

132 The NCEP/EMC StageIV is a precipitation estimation product, developed using hourly and  
133 6-hourly radar-rain gauge precipitation analyses at regional scales (Lin and Mitchell, 2005). In  
134 complex terrain, it is known that radar QPE suffers from the blockage of topography, overshooting  
135 and retrieval uncertainties, leading to large uncertainties in rainfall estimation. In 2007, as part of  
136 the ground validation (GV) of the Precipitation Measurement Missions (PMM) program by NASA  
137 (e.g., Prat and Barros, 2010a and 2010b), 34 tipping bucket rain gauges were installed in the  
138 Southern Appalachians and have been well-maintained since 2007 (e.g., Barros et al., 2014). In  
139 this work, rain gauge measurements from a GV rain gauge network in the Southern Appalachians  
140 are utilized to reduce StageIV uncertainties.

### 141 **2.2 GV Rain Gauge Observations**

142 A rain gauge network in support of PMM GV was installed in the Pigeon River basin for  
143 the 10 year 2007-2018 period (Barros et al. 2014). A map of this rain gauge network is plotted in

144 Figure 1. Every rain gauge is labelled with a number, and exact locations are documented in Table  
145 1. This rain gauge network is regularly visited and maintained at least three times a year, including  
146 on-site cleaning and calibration. In this study, these rainfall measurements are used as a basis to  
147 adjust hourly StageIV QPE. Note these rain gauge measurements can be downloaded at  
148 <http://dx.doi.org/10.5067/GPMGV/IPHEX/GAUGES/DATA301> (Barros et al., 2017). Besides  
149 rain gauges, a network of Parsivel disdrometers was installed during 2013-2014, with each  
150 disdrometer location denoted by the letter P in Figure 1. These disdrometer data were only used  
151 for independent evaluation because of short records. It is worth noting that rain gauges are installed  
152 mostly along the ridges while disdrometers are generally located at lower elevations.

153

154 <Figure 1 here please>

155

## 156 **2.3 Methodology**

157 The methodology of this work includes three major components: 1) rain gauge bias  
158 correction, 2) grid-scale QPE correction by closing the water budget using stream gauge  
159 measurements, and 3) basin and event selection procedures and model setup.

### 160 **2.3.1 Rain gauge Bias Correction**

161 Figure 2 shows a schematic drawing of the rain gauge bias correction framework to derive  
162 gauge-improved QPE (named StageIV<sub>DBKC</sub>).

163 <Figure 2 here please>

164

Formatted: Font color: Custom Color( RGB(51,51,255) )

165 First, to make meaningful comparison between StageIV and rain gauges in space, a fractal  
166 downscaling algorithm is used to create StageIV<sub>D</sub> at 1km from the original StageIV at 4 km  
167 resolution. Subsequently, bias correction using rain gauge measurements is employed to create  
168 StageIV<sub>DB</sub> at hourly timescales. StageIV<sub>DB</sub> data are evaluated against the rain gauge climatology  
169 from 2008 to 2017 to reduce biases that depend on weather regime, and climatological biases are  
170 then interpolated using the ordinary Kriging method. The resulting dataset is named StageIV<sub>DBKC</sub>  
171 (abbreviated as STIV<sub>DBKC</sub>).

172

### 173 2.3.2 Fractal downscaling

174 The methodology for fractal downscaling was first proposed by Bindlish and Barros (1996)  
175 and subsequently demonstrated through various applications to precipitation downscaling from  
176 models (Bindlish and Barros, 2000) and remote sensing data (Nogueira and Barros, 2015; Tao and  
177 Barros, 2010). Here, a brief description is presented.

178 The assumption of self-similarity is the basis for the fractal downscaling approach. The  
179 key parameters used in this approach include: the fractal dimension  $D$ , the Hurst coefficient  $H$ , and  
180 the spectral exponent  $\beta$  that are related through the following equations:

$$181 \quad D = \frac{7-\beta}{2} \quad (1)$$

$$182 \quad H = \frac{\beta-1}{2} \quad (2)$$

183 The parameter  $\beta$  describes rainfall statistics across different spatial scales, and it is  
184 calculated as the slope of the power spectral density curve in the 2D Fourier domain of the rainfall  
185 field (log-log plot). The parameter  $H$  is the Hurst coefficient which is a measure of autocorrelation

186 strength with higher value representing stronger autocorrelation. The power spectral density of a  
 187 2D field in Fourier domain is calculated as the following:

$$188 \quad Z(u, v) = \left(\frac{L}{N}\right)^2 \sum_{x=0}^{N-1} \sum_{y=0}^{N-1} z(x, y) \exp\left[-\frac{2\pi i}{N}(ux + vy)\right] \quad (3)$$

189 where N is the total number of grid points of the rainfall field z(x,y) with grid size being  
 190 the L, u and v correspond to frequency indices in the Fourier domain in each direction. The  
 191 averaged power spectral density is given:

$$192 \quad S_j = \frac{1}{L^2 N_j} \sum_1^{N_j} |Z(u, v)|^2 \quad (4)$$

193 where  $N_j$  denotes the number of points that meet the following condition:  $j < \sqrt{u^2 + v^2} <$   
 194  $j + 1$ . There is roughly a power-law relationship between the wavenumber k and the mean power  
 195 spectral density, and k is defined as below:

$$196 \quad k = \frac{2\pi}{\sqrt{u^2 + v^2}} \quad (5)$$

$$197 \quad S \sim k^{-\beta-1} \quad (6)$$

198 Specifically, the corresponding S value when wavenumber k = 1 is referred to as the  
 199 roughness factor, which is a representation of the variance of the field.

200 Assuming rainfall fields have self-similar statistics in the range of scales of interest, then  
 201 fine scale rainfall fields can be generated from available coarse scale fields by preserving these  
 202 self-similar statistics. This is done by generating a Brownian surface at desired fine scale resolution  
 203 while sharing the same spectral slope and roughness factor as the original rainfall field based on  
 204 Bindlish and Barros (1996):

205 
$$Z_D(u, v) = \frac{Z_b(u, v)}{k_r^{(\beta - \beta_b)/2}} \exp \left[ \frac{1}{2} \left( S_{r,1} - \frac{\beta + 1}{\beta_b + 1} S_{r,2} \right) \right] \quad (7)$$

206 where  $\beta$ ,  $\beta_b$ ,  $Z_D(u, v)$  and  $Z_b(u, v)$  are the spectral slope of 2D original rainfall field, the  
 207 spectral slope of the Brownian surface, interpolation surface in the Fourier domain and original  
 208 Brownian surface, respectively;  $k_r$  is the wavenumber and  $S_{r,1}$  and  $S_{r,2}$  are the roughness factors  
 209 of the 2D original rainfall fields and Brownian surface. Due to the non-uniqueness of Brownian  
 210 surfaces, an ensemble of ND interpolation surfaces  $Z_D$  is derived, and thus ND rainfall fields at  
 211 finer resolution preserving the same rainfall statistics at coarse resolution are generated. In this  
 212 work, a total of ND=50 ensemble downscaled rainfall fields are created like Nogueira and Barros  
 213 (2015). Because of the computational demands of the IRC (see Section 2.3.6) and the small area  
 214 of headwater basins that results in downscaled ensembles with narrow spread, the ensemble mean  
 215 of the 50 downscaled rainfall fields is calculated first, and subsequent rainfall bias correction steps  
 216 as described in Figure 2 are applied to the ensemble mean.

217

### 218 2.3.3 Bias Correction

219 The *first* phase of bias correction is carried out at the event scale: a linear regression is  
 220 established between rain gauge measurements and collocated downscaled radar pixel estimates  
 221 using the following formula:

222 
$$R_g^t(i_g, j_g) = \kappa R_r^t(i_g, j_g) + \varepsilon \quad (8)$$

223 where  $R_r$  and  $R_g$  represent radar and rain gauge measurements respectively,  $\kappa$  and  $\varepsilon$  are the  
 224 slope and the intercept of a polynomial fit between  $R_r$  and  $R_g$ . Hourly StageIV<sub>D</sub> estimates and  
 225 corresponding rain gauge observations in the same StageIV<sub>D</sub> pixel were identified if at least 2 rain

226 gauges in the same StageIV<sub>D</sub> pixel measure non-zero rainfall. A linear regression was applied to  
227 all StageIV<sub>D</sub> pixels within one standard deviation of the regression line at an hourly timescale by  
228 assuming homogeneity of variances or homoscedasticity.

229 The *second* phase of bias correction is done at decadal scale: aiming to reduce systematic  
230 radar errors caused by retrieval uncertainties and viewing geometry in complex terrain,  
231 demonstrating strong diurnal (time of day) and seasonal (weather regime) error dependencies due  
232 to miss detection of shallow rainfall systems related to radar overshooting in the Southern  
233 Appalachian when comparing against 10-year rain gauge observations (e.g., Wilson and Barros,  
234 2014; Arulraj and Barros, 2017). For this purpose, when rain gauge observations are <2mm/hr and  
235 Stage IV<sub>D</sub> estimates are 0mm/hr, the StageIV<sub>D</sub> value was replaced by the rain gauge observations,  
236 which is referred to as the Light Rainfall Correction (LRC). Moreover, if StageIV<sub>D</sub> estimates equal  
237 to 0 where at least one collocated rain gauge observation is >2mm/hr, then StageIV<sub>D</sub> estimates are  
238 replaced by the average of all collocated rain gauge observations, referred to as the Mean Rainfall  
239 Correction (MRC). Lastly, for highly localized precipitation (i.e., less than 2 rain gauges register  
240 nonzero rain in the study domain) which is normally associated with convective activity, the  
241 rainfall differences between the StageIV<sub>D</sub> and the local rain gauge observations were bilinearly  
242 distributed across (a 5x5 window centered at the StageIV<sub>D</sub> pixel, referred to as the Convective  
243 Rainfall Correction (CRC). Rainfall was recorded at more than 2 rain gauges for the majority of  
244 events, in which case the differences at each pixel between radar estimates and rain gauge  
245 measurements were spatially interpolated using a geostatistical interpolation method (e.g.,  
246 ordinary Kriging), referred to as the Global Rainfall Correction (GRC).

247

248 **2.3.4 Ordinary Kriging**

249 Ordinary Kriging is a geostatistical interpolation method that generates artificial values of  
 250 a variable at a specific location, aiming to minimize spatial variance. In this work, rainfall  
 251 differences between raingauge observations and StageIV<sub>DB</sub> are calculated and distributed across  
 252 the entire basin using a spatial variance model, specifically a spherical semi-variogram model.  
 253 Literature regarding the choice of semi-variogram models and their properties includes  
 254 Zimmerman and Zimmerman (1991), Li and Heap (2008), and Oliver and Webster (2015). Bohling  
 255 (2005) pointed out that spherical models reach the maximum variance for shorter spatial lags,  
 256 therefore more suitable to capture highly nonlinear and localized orographic precipitation  
 257 (McBratney and Webster, 1986):

$$258 \quad \gamma(h) = C_0 + (C - C_0) \left( \frac{3h}{2d} - \frac{1}{2} \left( \frac{h}{d} \right)^3 \right) \quad \text{if } 0 \leq h \leq d \quad (9.1)$$

$$259 \quad = C \quad \text{if } h > d \quad (9.2)$$

$$260 \quad \gamma_{0i} = \frac{1}{N_A} \sum_{k=1}^{N_A} \gamma_{ki} \quad (9.3)$$

$$261 \quad \gamma_{00} = \frac{1}{N_A} \sum_{k=1}^{N_A} \sum_{l=1}^{N_A} \gamma_{kl} \quad (9.4)$$

262 where  $h$  is the lag,  $d$  is the range,  $C$  and  $C_0$  are the sill and nugget values of the semi-variogram  
 263 model,  $N_A$  is the number of rain gauges. The nugget is assumed to be zero if local variability and  
 264 measurement error are neglected at the point scale (Diggle and Ribeiro, 2007). The interpolated  
 265 rainfall difference at a location  $x_0$   $Z_{ok}^*(x_0)$  is obtained using a weighted combination of all  
 266 available differences multiplied by Kriging weights:

$$267 \quad Z_{ok}^*(x_0) = \sum_{i=1}^n \lambda_i^{ok} G(x_i) \quad (10.1)$$

268 
$$\sum_{i=1}^n \lambda_i^{OK} = 1 \quad (10.2)$$

269 Optimal Kriging weights can be obtained by a series of linear equations using the Lagrange  
 270 multiplier  $\mu$  method:

271 
$$\begin{pmatrix} \gamma_{11} & \dots & \gamma_{n1} & 1 \\ \vdots & \ddots & \vdots & \vdots \\ \gamma_{1n} & \dots & \gamma_{nn} & 1 \\ 1 & \dots & 1 & 0 \end{pmatrix} \begin{pmatrix} \lambda_1^{OK} \\ \vdots \\ \lambda_n^{OK} \\ \mu \end{pmatrix} = \begin{pmatrix} \gamma_{01} \\ \vdots \\ \gamma_{0n} \\ 1 \end{pmatrix} \quad (11)$$

272 In this work, Ordinary Kriging interpolates differences between radar data and rain gauge  
 273 observations to produce gauge-corrected STIV<sub>DBKC</sub> dataset.

274

### 275 2.3.5 Precipitation Assessment Metrics

276 Assessment metrics include the following: bias and root mean square error between radar  
 277 estimation and rain gauge measurement, false alarm rate, the probability of detection, the threat  
 278 score and the Heidke skill score, following McBride and Ebert (2000). An instance when both  
 279 radar QPE and rain gauge observation exceed a specified rain rate threshold is a hit (H); when  
 280 observation matches the criterion and radar QPE does not, it is classified as a miss (M); if the  
 281 opposite happens, then it is a false alarm (FA). The calculation of these metrics relied on a  
 282 collection of Hs, Ms, and FAs:

283 
$$Bias = \frac{1}{N} \sum_{n=1}^N (O_n - R_n) \quad (12)$$

284 
$$RMSE = \sqrt{\frac{1}{N} \sum_{n=1}^N (O_n - R_n)^2} \quad (13)$$

285 
$$FR = \frac{FA}{H+FA}, 0 \leq FR \leq 1 \quad (14)$$

286 
$$PD = \frac{H}{H+M}, 0 \leq PD \leq 1 \quad (15)$$

287 
$$TS = \frac{H}{H+FA+M}, 0 \leq TS \leq 1 \quad (16)$$

288 
$$HSS = 2 * \frac{Z * H - FA * M}{((H+FA) * (Z+FA)) + ((M+H) * (M+Z))}, -1 \leq HSS \leq 1 \quad (17)$$

289 where O is the rain gauge observation, R is the radar QPE, and N is the number of points. Z  
 290 represents the number of zeros, meaning both rain gauge and radar do not register rainfall above a  
 291 predefined threshold. A threat score (TS) of 0.5 means over 50% of cases meet the criterion, and  
 292 the higher the better. An HSS of 0 means a forecast has the same performance as a random guess.

293

294 **2.3.6 Inverse Hydrologic Correction**

295 At flash flood timescales in headwater basins, streamflow uncertainty and precipitation  
 296 uncertainty are strongly connected in a nonlinear way through rainfall runoff processes. Liao and  
 297 Barros (2022) developed a Lagrangian-based framework named Inverse Rainfall Correction (IRC),  
 298 allowing backpropagating streamflow uncertainty to precipitation inputs in space and time through  
 299 an uncalibrated distributed hydrological model (i.e., DCHM), achieving water budget closure at  
 300 the event scale in small headwater basins. As stated earlier, the uncertainties associated with  
 301 parameters and structural uncertainty of the hydrological model DCHM are considered negligible  
 302 since the model configurations have been used and improved over the past two decades for this  
 303 region accounting for various soil, vegetation, and river processes (e.g., Tao and Barros, 2013,  
 304 2014, 2018 and 2019; Yildiz and Barros, 2005 and 2007; Lowman and Barros, 2016), and the IRC

305 framework has been tested in multiple headwater basins extensively in this region with consistent  
306 success. A detailed description of the IRC is provided in Section 2.3.8 and Appendix A.

307         The IRC is a general framework to improve QPE at the watershed scale that can be  
308 incorporated into any distributed hydrological models. Liao and Barros (2025a, 2025b)  
309 investigated the impact of model structure uncertainty and initial conditions uncertainty on the  
310 IRC and: the resulting IRC-improved QPE. The results suggest that with improved watershed  
311 physics at finer resolution (e.g., river bank storage, Liao and Barros, 2025a), improved routing  
312 algorithms for steep river channels (e.g., XY routing, Liao and Barros, 2025a), and improved soil  
313 moisture initialization (Liao and Barros, 2025b), the post-IRC QPE demonstrate realistic  
314 precipitation features at high resolution that are aligned with basin topography with ridges  
315 associated with higher precipitation than valleys in general, showing a significant improvement  
316 from the original StageIV dataset which is characterized by unnatural boxy precipitation patterns  
317 in complex terrain due to resolution issues and over or underestimation depending on topography  
318 and distance from the radar site.

319         As briefly mentioned before, LB22 reviewed various sources of uncertainty that can  
320 prevent post-IRC QPE from achieving water budget closure, among which initial condition  
321 uncertainty in soil moisture is a noteworthy source. Improved initial condition estimation results  
322 in significantly improved post-IRC precipitation features in complex terrain by better capturing  
323 transient travel time distributions (Liao and Barros, 2025b). They found that the uncertainty tied  
324 to initial conditions is more significant for less extreme events. Nevertheless, the initial condition  
325 correction method is coupled with the IRC framework, and the precipitation products are named  
326 after the IRC-ICC framework. The specifics regarding the IRC, ICC, and IRC-ICC are  
327 schematically drawn in Figure 3.

328

329 <Figure 3 here please>

330

331 Using the definitions of characteristic timings shown in panels c) and d), characteristic flow  
332 regime windows are identified. In principle, the number and the size of the windows depend on  
333 the complexity of the hydrograph. ICC is only applied to windows 2 and 5 in this example, which  
334 represents a segment of the hydrograph characterized by the differences between rising points in  
335 observations and simulations, and a segment characterized by slow recession, respectively. The  
336 assumption is that precipitation uncertainty regulates streamflow differences during peak flows  
337 (i.e. windows 3 and 4).  $W_{nm}$  represents the framework state after window  $m$  for iteration  $n$ . The  
338 resolution settings for the DCHM are: spatial resolution: 250m, and temporal resolution: 5 minutes.

### 339 **2.3.7 Implementation of Lagrangian Tracking**

340 A flood event is simulated by the DCHM at the basin outlet with grid-based time-varying  
341 velocity fields for different soil layers. When the precipitation starts (i.e. basin-averaged  
342 precipitation  $> 0.1\text{mm/hr}$ ), new particles (passive tracers) are launched at the same frequency of  
343 model temporal resolution (5 minutes), but only at non-zero precipitation grids in all soil layers  
344 following the velocity fields calculated by the DCHM, and the tracking resolution is 10 seconds,  
345 amounting to a release of approximately 600,000 particles for basin with an area of  $120\text{km}^2$  over  
346 a 24-hour period. During the tracking phase, each particle is saved along with information  
347 regarding its source location (grid-point where it originates), time of release  $t_i$ , and travel time  $t_T$   
348 ( $t_T$  is defined as the difference between current time  $t$  and the time of release  $t_i$ , i.e.,  $t_T = t - t_i$  ).  
349 Multiple particles from different source locations can have the same travel time, which is the basis

350 for identifying the number of trajectories contributing to the hydrograph at the outlet as a function  
351 of time.

352

### 353 2.3.8 QPE Correction Using IRC

354 At time  $t$ , the water difference  $wd(t)$  between the observed and simulated streamflow over  
355 the time  $\Delta t$  between two consecutive discharge observations represents the fraction of runoff that  
356 eventually leaves the basin as streamflow. Errors in precipitation forcing propagate to the runoff,  
357 under the assumption of negligible model and parameter uncertainties,  $wd(t)$  can be entirely  
358 attributed to precipitation error, which is the focus of this work.

$$359 \quad wd(t) = [Q_{obs}(t) - Q_{simu}(t)] \times \Delta t \quad (18)$$

360 The subscripts *obs* and *simu* refer to observed and simulated discharge, respectively.  
361 The strategy for the inverse rainfall correction (IRC) using hydrograph analysis is to follow  
362 backward the trajectories available from the Lagrangian tracking from the basin outlet to the  
363 source locations at time  $t_i$  and apply a correction at the source locations proportional to the original  
364 QPE magnitude to reduce  $wd$  at time  $t$ . Detailed formulas with a conceptual drawing can be found  
365 in Appendix A. The embedded assumption is that larger QPE values have larger uncertainties.  
366 Note that QPE corrections that happened earlier in time will have an impact on runoff simulation  
367 at future times, and this is the reason why the IRC framework is a recursive framework. The  
368 detailed rainfall correction steps can be found in (Liao and Barros, 2022).

369

370 **2.3.9 Methods for Reducing Uncertainties from Other Sources**

371 As briefly mentioned above, uncertainties from multiple sources (e.g., model physics,  
372 model numerical formulation, antecedent soil moisture conditions, etc.) impact travel time  
373 distributions and simulated streamflow to a higher or lesser degree depending on location,  
374 antecedent conditions, and storm system. Previous studies demonstrated that, for flood-producing  
375 events in small headwater basins, streamflow response is largely controlled by precipitation inputs  
376 (e.g., Iwasaki et al., 2020). In this section, we briefly describe the methods used to minimize the  
377 impacts from other sources to enhance water budget closure using the IRC approach.

378 As discussed in the Introduction, DCHM has been used in the Appalachian Mountains at  
379 event-scale (e.g., Tao and Barros, 2013, 2014, 2018 and 2019; Tao et al. 2016) and at seasonal and  
380 interannual scales (Yildiz and Barros 2005, 2007 and 2009), and thus extensive analysis of  
381 parameter uncertainty and model structure uncertainty has been conducted previously. Recent  
382 improvements to the flood routing algorithm have resulted in significant improvements in flood  
383 peak timing in headwater basins to reconcile the hydraulics of flood wave propagation on steep  
384 slopes at the highest elevations with milder slopes at intermediate elevations in the valleys (Liao  
385 and Barros, 2025a). Their results also suggest meandering effects, riverbank storage, and initial  
386 soil moisture distributions can impact the early rising period of the hydrographs. Significant and  
387 consistent improvements are made when introducing an initial condition correction (ICC) module  
388 to reduce initial condition uncertainty (Liao and Barros, 2025b). This innovative ICC module is  
389 coupled with the IRC framework. The red arrows in Figure 3e indicate where ICC is executed in  
390 the general architecture of the IRC framework, and the specifics of the ICC module are described  
391 below.

392 Particles launched during the IRC process that reached the outlet at time  $t$  are traced back  
393 directly to the IC timing or time 0, and their locations at the IC time are shown in the bottom maps  
394 in Figure 3d (referring to control points of time  $t$ ). The downstream area of the control points has  
395 shorter transport time to arrive at the outlet (e.g., water difference  $\Delta S_1$ ), and the upstream area of  
396 the control points takes longer to get to the basin outlet (e.g., water difference  $\Delta S_2$ ). Similarly, soil  
397 moisture in the impacted area can greatly impact the size of  $\Delta S_2$  and flow conditions after the  
398 timing  $t_2$ . Assuming initial conditions are only impactful during the early period and late recession  
399 of the hydrograph, which is supported by the fact that these events are flood-producing events with  
400 large QPE uncertainties dominating the vicinity of peak flow, ICC is used for hydrological  
401 windows outside the peak flow windows. Following the same notation (backward-in-time) in the  
402 IRC framework (Eq. 18),  $wd(t)$  is calculated as the flow volume difference between observed and  
403 simulated streamflow for the time interval defined by  $t$  and  $t - \Delta t$ . A ‘band’ can therefore be  
404 identified, that is, a region formed by control points of time  $t$  and control points of time  $t - \Delta t$ .  
405 This ‘band’ is then referred to as the impacted area of initial soil moisture for time  $t$ , meaning that  
406 the basin discharge between time  $t - \Delta t$  and time  $t$  is impacted by initial soil moisture at the  
407 delineated impacted area. Finally,  $wd(t)$  is then converted to soil moisture content and added to  
408 initial soil moisture within the impacted area (i.e. the ‘band’) and the details can be found in Liao  
409 and Barros (2025b).

410

### 411 2.3.10 Hydrological Skill Metrics

412 The Kling-Gupta Efficiency (KGE) is calculated using observed and simulated streamflow  
413 statistics at observation resolution  $\tau$  (here 15 minutes) in this work:

414 
$$KGE_{\tau} = 1 - \sqrt{(r - 1)^2 + \left(\frac{\sigma_{sim}}{\sigma_{obs}} - 1\right)^2 + \left(\frac{\mu_{sim}}{\mu_{obs}} - 1\right)^2}$$
 (19)

415 where  $r$  is the correlation between simulations and observations,  $\sigma_{obs}$  is the standard  
 416 deviation of observed discharge,  $\sigma_{sim}$  is the simulated discharge standard deviation,  $\mu_{sim}$  and  
 417  $\mu_{obs}$  represent the average simulated and observed streamflow values, respectively.

418 The relative volume error (EV) is the relative difference between simulated flood volume  
 419 and observed flood volume:

420 
$$EV = \frac{V_{sim} - V_{obs}}{V_{obs}}$$
 (20)

421 Where V stands for volume of the flood. An  $EV > 0$ , and an  $EV < 0$  mean overestimation and  
 422 underestimation, respectively.

423 EPT refers to the error in peak flow timing between observations and simulations. For its  
 424 calculation, only the highest peak is selected for calculating EPT if more than one peak is present.  
 425 In this work, EPT is determined by considering the entire flood rising limb to account for the  
 426 steepness of the rising limb, specifically, both the flood started timing and the maximum flood  
 427 timing from the flood front rising limb are used for calculating the EPT.

428 EPV or error in peak volume ( $Q_{max}$ , cubic meters per second) is a relative error calculated  
 429 using peak flows from observations and simulations, and the equation is below:

430 
$$EPV = \frac{Q_{max_{sim}} - Q_{max_{obs}}}{Q_{max_{obs}}}$$
 (21)

431

432 **2.3.11 Study Domain and Model Setup**

433 Twenty-eight headwater basins are selected in the Appalachians as illustrated in Figure 1,  
434 with basin drainage area ranging from 50 km<sup>2</sup> to 500 km<sup>2</sup>. It is demonstrated in Figure 4 that these  
435 basins scatter across the entire Appalachians. For example, Basin01 and Basin30 are over 2,000  
436 km apart, with diverse weather and climate regimes, and large differences in geomorphology and  
437 hydrogeology.

438

439 <Figure 4 here please>

440

441 Soil-related parameters are downloaded from a global high-resolution (1 km) soil data  
442 repository (Zhang et al., 2018). For each basin, the vertical hydraulic conductivity remains the  
443 same for the entire soil column. The lateral hydraulic conductivity in the unsaturated zone was  
444 assumed to be two to three orders of magnitude larger than the vertical conductivity in the shallow  
445 soil layers, with higher values where the stone fraction in the soils is higher (Carlson, 2010; Freeze  
446 and Cherry, 1979). The final scaling factors were obtained through simple sensitivity analysis to  
447 match the curvature and slope of the observed subsurface runoff recession curves (e.g., Linsley et  
448 al., 1982; Chen and Kumar, 2001; Yildiz and Barros, 2007), and scaling factors are finally  
449 determined as: 1500, 150, 15 and 1.5 for layer 1 (0-10 cm below terrain surface), layer 2 (10-75  
450 cm below terrain surface), layer 3 (75-200 cm below terrain surface) and layer 4 (2-20 m below  
451 terrain surface), respectively. No parameter optimization is done in this work, as the primary focus  
452 of this work is to develop a QPE dataset that can consistently close the water budget while

453 controlling uncertainties from other sources, largely advancing the understanding of QPE  
454 uncertainties across climate, weather, and geomorphological regimes.

455 Flood-producing events have been selected for the 28 headwater basins for recent years  
456 from January 2021 to April 2024. A qualified event is determined based on the observed peak  
457 flow, which must surpass 95% of available flow measurements for each basin. The choice of 95%  
458 is a compromise because 99% would yield too few events, while 90% would be too close to the  
459 annual flood. Additionally, rainfall runoff response time must be shorter than or equal to 6 hours  
460 to be qualified as a flash flood event. Only warm season precipitation events from 2021 to 2024  
461 are finally considered. Here, the warm season is specifically defined as from April 1st to September  
462 30th. Note: data quality control is enforced, and events with missing streamflow records are  
463 discarded.

464 For the Cataloochee Creek Basin (Basin05), located in the SAM known to have  
465 experienced multiple flash floods in the past (Tao and Barros, 2013 and 2014), Liao and Barros  
466 (2023) created a Historical Flood Record database (HFR) that includes a large number of extreme  
467 rainfall events from 2008 to 2017. The event selection criteria when developing HFR also use the  
468 same 95% flow threshold method. The difference is that the HFR also includes multiple winter-  
469 time liquid precipitation events that result in cold-season flash floods. In total, there are 54 warm-  
470 season events for Basin 05 in HFR, and these events are also used to expand the study sample size  
471 in this work.

472 To warm up the DCHM, a traditional spin-up approach is used with iterative runs for the  
473 hydrological year of 2021 (from the end of April to the end of September), and it generally reaches  
474 equilibrium after 3-5 iterations. Subsequently, DCHM is continuously running from the beginning  
475 of October 2021 onwards, to derive initial conditions for events after September 30th, 2021.

476 During this spin-up process, no parameter calibration is involved. The initial conditions are  
477 extracted from the last iteration of spin up run, and the following model outputs generated after  
478 October 1<sup>st</sup>, 2021.

#### 479 **2.4 Caveats**

480 In the entire study domain, rain gauges are only installed in the Southern Appalachians,  
481 specifically in the vicinity of the Cataloochee Creek Basin (Basin 05). However, the rest of the  
482 regions are not equipped by raingauge networks, and therefore, no rain gauge bias correction is  
483 done for those basins, and the downscaled original dataset StageIV (i.e., STIV<sub>D</sub>) is used as input  
484 for the IRC method and hydrological simulations in this study.

485 As an important component of the IRC framework, the Lagrangian tracking algorithm is  
486 only implemented when hydrological window changes, rather than following model temporal  
487 resolution (i.e., 5 minutes), due to practical computational constraints. Additionally, we do not  
488 differentiate peak flow points and recession inflection points between simulations and observations  
489 when classifying hydrological flow regimes/windows, and consistently use observations delineate  
490 hydrological windows simply because 1) particle locations are inherently much more uncertain  
491 when simulation time is getting longer partially due to numerical truncation errors and grid-based  
492 abruptly-changing velocity fields used in the Lagrangian tracking algorithm, and 2) the  
493 computational costs of the tracking algorithm. Very short travel times (i.e., <15 minutes) are  
494 ignored because of temporal resolution restrictions from streamflow observations. A systematic  
495 use of 24 hours for event total duration is imposed in this work to reduce excessive tracking  
496 workload, which might be problematic for events with very long and heavy tails, though not  
497 common for flash flood events in headwater basins.

498 The IRC-ICC recursive framework allows us to quantify QPE uncertainties more  
499 realistically by improving initial soil moisture estimation, and this framework is numerically  
500 efficient in terms of reaching hydrological equilibrium within 3-5 iterations. In this work, stable  
501 IRC-ICC precipitation is reached when the KGE changes are bound by 0.05.

### 502 **3. Results and Discussion**

#### 503 **3.1 Rain gauge Bias Correction**

504 The climatologically corrected  $STIV_{DBKC}$  fields have a significantly accurate diurnal cycle  
505 compared to only event-scale bias-corrected  $STIV_{DBK}$ . This process is illustrated in Figure 5 for  
506 one rain gauge from each side of the ridges (eastern side: left panel; western side: right panel) in  
507 the Southern Appalachians.

508

509 <Figure 5 here please>

510

511 Original  $StageIV_D$  show higher biases over the western ridges (e.g., right panel) for all hours of  
512 day, illustrating the difficulties of capturing seeder-feeder enhancement of low-level precipitation  
513 systems (Duan and Barros, 2017). Also, the mid-day dry bias has been a problem for radar  
514 measurements in this region. (e.g., Barros and Arulraj, 2019). Results show that  $StageIV_{DBKC}$   
515 datasets capture precipitation climatology better with smaller missing detection errors compared  
516 to original  $StageIV$ . Figure 6 shows the diurnal characteristics of the missing percipitaaion for  
517 two raingauge locations for winter season (January-February and March – JFM) using  $StageIV$ ,  
518 and this phenomon is observed for both the  $StageIV_D$  (black) and  $StageIV_{DBK}$  (cyan). These  
519 missing cases correspond to light rainfall that has small rainfall measurements at rain gauge

520 locations ( $< 1.5$  mm/hr, bottom row). After applying precipitation climatology corrections, the  
521 missing issue in StageIV<sub>DBK</sub> is significantly alleviated and much better results are shown in  
522 StageIV<sub>DBKC</sub> fields (green).

523

524 <Figure 6 here please>

525

526 The seasonal HSS, TS, and RMSE of STIV<sub>DBKC</sub> are significantly better than those of  
527 STIV<sub>D</sub> throughout the day using 10-year averages (Figure 7a). It is worth noting that with  
528 increasing precipitation rate threshold (Figure 7b), threat score does not show decreasing trend,  
529 meaning rain gauge bias correction for heavy rainfall events works well. Figure 7c shows RMSE  
530 performance conditional on rain rate at diurnal and seasonal scales. Overall, the RMSE is generally  
531 less than 0.1 mm/hr except in the cold-season morning and late afternoon, which can be partially  
532 attributed to snow events because these rain gauges are not heated.

533

534 <Figure 7 here please>

535

### 536 **3.2 Hydrologic Correction**

537 The coupled IRC-ICC was originally developed and applied in Basin 05, the Cataloochee Creek  
538 Basin, and an example showing the results from iterations is demonstrated in Figure 8. The  
539 notation follows the definition in Figure 3. Note that the STIV<sub>DBKC</sub> data derived in Section 3.1 are

540 further downscaled to 250m and used for hydrological simulations in this section. For all other  
541 basins (except Basin05), rain gauges are not available, and STIV<sub>D</sub> data are used instead.

542

543 <Figure 8 here please>

544

545 The IRC-ICC produces stable results after about 3 to 4 iterations without significant oscillations  
546 for this specific extreme flood event. In general, for less significant events, IRC-ICC reaches  
547 equilibrium faster (merely three iterations), providing fast and convergent corrections. As  
548 explained earlier, the equilibrium state is reached and thus IRC-ICC is stopped when oscillations  
549 in simulated KGE are within 0.05, and then IRC-ICC is stopped immediately. This study suggests  
550 that for most events, three iterations is a good rule of thumb. The difference between the initial 4D  
551 (x, y, z, t) rainfall forcing and the final result of the IRC-ICC is the general IRC correction.

552

### 553 **3.2.1 Systematic Application of IRC-ICC**

554 The IRC-ICC is systematically executed in the 28 basins located in the Appalachians for  
555 225 events. Examples are displayed in Figure 9.

556

557 <Figure 9 here please>

558

559 Simulated streamflow generally has better performances in the Northern and Southern  
560 Appalachian Mountains (NAM, SAM) compared to the Central Appalachian Mountains (CAM).

561 Specifically, in the Karst region along the interstate border of Virginia and West Virginia in the  
562 CAM, for Basins 13 and 14, where there are numerous caverns and natural tunnels facilitating  
563 fast subsurface flow response, that is, sinking and subterranean streams  
564 (<https://www.dcr.virginia.gov/natural-heritage/vacavetrail>) and  
565 <https://docslib.org/doc/2284608/west-virginia-tax-districts-containing-karst-terrain>). The current  
566 version of the DCHM does not have a specific module designed for karst geology and karst  
567 hydrological processes. Thus, the IRC-ICC results in these locations are impacted by model  
568 structural uncertainty. Here, the advantage of not calibrating model parameters becomes apparent.  
569 It would be possible to calibrate model parameters to improve model simulations; however, the  
570 physical basis and transferability of the IRC-ICC results would be compromised. The 10 events in  
571 Basins 13 and 14 are therefore discarded (example: Figure A3). This point of discussion is  
572 highlighted here to reinforce the value of the data set presented in this manuscript for applications  
573 with other hydrologic models, including model calibration, where model structural uncertainty is  
574 not a primary concern at resolved scales.

575       Event 2021-06-10 in Basin 19 (see Figure A3) is an example of an event with a complex  
576 hydrograph (e.g., multiple minor flood peaks around one major flood peak) that requires more  
577 hydrological windows (see Figure 3). Subtle changes in the shape of the hydrograph could be  
578 indicative of spatial shifts in runoff production from one tributary to another following the track  
579 of storm cells over the basin. Indeed, depending on the weather system and regional topography,  
580 the travel velocity of such cells and their life cycle may require finer spatial and temporal resolution  
581 both for the hydrological model and for the tracking algorithm to capture changes in the spatial  
582 structure of precipitation, especially in the case of summer thunderstorms. For the systematic  
583 production of this data set, a 5-window IRC-ICC framework was applied, including a pre-rising-

584 point segment, rising limb, early recession, and late recession (separated by the recession inflection  
585 point).

586

### 587 **3.2.2 IRC and IRC-ICC Precipitation Corrections**

588         Accumulated rainfall totals per rainfall event are calculated for both the IRC-only product  
589 and post IRC-ICC products. Subsequently, these rainfall totals are directly compared against the  
590 original product STIV<sub>DBKC</sub>. Examples are shown in Figure 10, categorized by seasons in the  
591 Cataloochee Creek Basin (Basin05). Again, the warm season is defined as April 1st to September  
592 30th, and the remaining events are defined as the cold season, with only liquid precipitation events  
593 studied in this work.

594

595 <Figure 10 here please>

596

597         The original QPE (**a1** and **b1**) fields show abrupt changes in rainfall intensity, ‘boxy’  
598 patterns, which is a common issue of radar observations at high spatial resolution. On the contrary,  
599 the IRC-corrected precipitation maps demonstrate precipitation features aligning with landform,  
600 showing strong spatial precipitation gradients along ridges and adjacent valleys (examples are  
601 listed in Figure A2). The spatial correlation between orographic precipitation and topography is  
602 observed across all mountain ranges, including the Appalachians (e.g., Konrad II, 1994; Smith et  
603 al., 2011; Wolvin et al., 2024). Note the dark blue colors in Figure 10 corresponding to very low  
604 precipitation near the basin outlet. These are an artifact of the IRC tied to very short travel times  
605 that cannot be fully resolved even at fine scales of 250m and 5minutes. However, these artifacts

606 are much reduced for the IRC-ICC due to the reduction of uncertainty in initial conditions, as  
607 shown for the 2009-10-14, 2009-04-20, and 2013-04-12 events because of overall basin-wide  
608 travel-time improvement. It is worth noting that these three events are relatively mild events,  
609 indicating a larger impact of IC on relatively less extreme events because of the critical role of IC  
610 in runoff generation mechanisms and travel times distributions. Thus, the extreme event  
611 precipitation product obtained from IRC-ICC is the data set recommended for applications and  
612 intercomparison studies with other hydrologic models. [Because the IRC is always applied with](#)  
613 [ICC following Liao and Barros \(2025b\), we refer to the IRC-ICC precipitation product as IRC for](#)  
614 [simplicity.](#)

615

### 616 3.2.3 Precipitation and Hydrologic Statistics

617 Event-total precipitation maps are calculated for each basin and event, and basin-scale  
618 precipitation statistics (e.g., mean and standard deviation) are derived for each event-total  
619 precipitation map. These statistics are plotted in Figure 11, and subregions are separated by vertical  
620 black lines. Basins 01 to 11 are located in the SAM, Basins 12 to 20 are in the CAM, and Basins  
621 21 to 30 are located in the NAM. Basins 13 and 14 are not included in the statistics.

622 <Figure 11 here please>

623 It is clearly demonstrated that the change in the mean (i.e., basin-averaged event total QPE)  
624 is relatively small (from 36.10mm to 38.07mm) compared to the change in the standard deviation  
625 (from 6.63mm to 14.08mm) after the application of IRC-ICC. The small standard deviation of the  
626 original QPE suggests that the original QPE data are spatially tightly clustered with low variability  
627 (see Figure 10a for boxy rainfall features), while the larger standard deviation post-IRC-ICC

628 indicates spatial variability is enhanced, which is highlighted by the terrain-aligned precipitation  
629 features in Figure 10c. The relatively small change in the mean indicates that the original input  
630 precipitation (i.e., StageIV<sub>DBKC</sub> for Basin 05, and StageIV<sub>D</sub> for the remaining basins) does not  
631 contain significant unconditional systematic biases across basins and events, which would lead to  
632 consistent positive or negative flood volume errors. As an exception, it is worth noting that the  
633 standard deviation of Basin 05 events does not change significantly after the IRC-ICC compared  
634 to other basins and events because rain gauge corrections from the IPHEX network are employed  
635 in Basin 05 but not anywhere else. It can never be emphasized that even after rain gauge bias  
636 correction, essentially a point-scale correction method, the resulting flood hydrograph exhibits  
637 significant water budget closure errors (see Figure 12 for more discussion) on account of the high  
638 heterogeneous nature of QPE in complex terrain.

639 The hydrologic statistics described in Table 1 using all studied events are plotted in Figure  
640 12.

641 <Figure 12 here please>

642 Figure 12 shows that the median KGE across events is improved from 0.36, 0.39, 0.27 to  
643 0.89, 0.74, 0.84 for SAM, CAM, and NAM, respectively. It should be pointed out that QPE  
644 changes for Basin 05 events (event numbers 55 to 108) are important for improving water budget  
645 closure, albeit small in magnitude compared to other events in other basins, as shown in Figure 11  
646 and 12, and yet critical to capture the complex precipitation heterogeneity in complex terrain to  
647 close the water budget. The results for Basin 05 illustrate the limitations of rain gauge-based bias  
648 corrections in complex terrain in general. The relatively small improvement shown in the CAM is  
649 partially attributed to the fact that DCHM does not have a representation of subterranean rivers in  
650 karst terrain, causing large baseflow errors during hydrograph recession and thus low KGE values.

651 Nevertheless, for flash flood applications, peak flow magnitude, flood flow timing, and event flow  
652 volume are the most important forecast objectives, corresponding to the 2<sup>nd</sup>, 3<sup>rd</sup>, and 4<sup>th</sup> horizontal  
653 panels in Figure 12. Overall, flood volume error (EV) is controlled within  $\pm 10\%$  for over 90% of  
654 the studied events (the 2<sup>nd</sup> panel), with the median EV error being less than 5% in the SAM and  
655 NAM after IRC-ICC corrections. Flood peak volume (the 3<sup>rd</sup> panel) is generally controlled within  
656 20%, which is very good for extreme events in regions without ground-based observations except  
657 for radars placed far away. This is demonstrated by Tropical Storm Fred on 2021-08-17: an event  
658 that caused floods in multiple SAM basins, caused five deaths, and resulted in an economic loss  
659 of more than 1 billion dollars. Note the KGE for this event is improved to 0.9, and peak timing  
660 errors are  $< 30$  minutes using IRC-ICC. Timing errors (shown in the 4<sup>th</sup> subplot) are bounded by  
661  $\pm 60$  minutes for the major of the events for post IRC-ICC datasets, though some outliers exist  
662 potentially due to complex antecedent land surface physics (e.g., rain on snow) for April events,  
663 particularly in the CAM and NAM.

664 Events associated with significant timing errors (more than  $\pm 90$  minutes) are investigated  
665 in detail. These include the 2023-07-08 event (event number 185) for Basin 27, in New Hampshire  
666 (the estimated flood front occurs too early by 2.5 hours). This was a localized summer  
667 thunderstorm event, only taking 30 minutes to reach its peak flow. The fast changes in the  
668 hydrological regime require much more windows than the current classic 5-window settings used  
669 in the IRC-ICC framework. The event on 2022-05-27 (event number 118) in Basin16 located in  
670 West Virginia is characterized by a slow rising limb. Note Basin16 is partially located in a complex  
671 region with karst features (e.g., sink holes) in the Greenbrier-river valley. Finally, the event 2021-  
672 09-22, a complex rainfall system characterized by multiple rain cells passing through the Basin 19  
673 quickly (event number 133), requiring smaller hydrological windows to capture highly variable

674 rainfall-runoff responses than the 5-window default IRC-ICC architecture: baseflow segment, pre-  
675 rising segment, flood rising limb, early and late recession.

676 Overall, large improvements in QPE are achieved, resulting in hydrological improvements  
677 in aspects of peak magnitude, flood total volume and flood front timing. Due to the dependence of  
678 IRC-ICC on travel time distributions, it cannot be used when precipitation is missing or there are  
679 severe timing errors because of the lack of water travel time trajectories to distribute corrections.  
680 From a practical point of view, the QPE IRC-ICC correction is in nature a type of space-time bias  
681 correction. The improved QPE data facilitates the development of QPE error models, which is  
682 demonstrated by the same authors (e.g., Liao and Barros, 2023), providing a path towards  
683 correcting remote-sensing products to support hydrometeorological studies and advancing the  
684 calibration of hydrological models with significantly less forcing uncertainty.

685

#### 686 **3.2.4 Independent Verification**

687 As mentioned in the introduction, precipitation measurements are limited in the Appalachians  
688 except for the IPHEX rain gauge network (Figure 1). Currently, the NEXRAD radar network  
689 remains the widely used precipitation monitoring system in this region in spite of well-documented  
690 low radar quality coverage over radar gaps in the mountains. The Multi-Radar/Multi-Sensor  
691 (MRMS) product (Zhang et al., 2016), which is developed using NEXRAD radar measurements  
692 similar to StageIV, is created at 1km resolution and is used here for independent verification.

693 First, original MRMS data are downscaled to the same resolution as StageIV<sub>D</sub> datasets (250m,  
694 5min) and used as inputs for DCHM. Hydrological simulations in this section are using the same  
695 model configuration and initial model states for the purpose of a meaningful comparison, including

696 the following datasets: MRMS<sub>D</sub>, StageIV<sub>D</sub>, and IRC-ICC StageIV<sub>D</sub> as shown in Figure 13. Figure  
697 13a shows that MRMS and StageIV QPE have similar results. Second, the IRC-ICC StageIV<sub>D</sub>  
698 have generally a good agreement with MRMS<sub>D</sub> similar to StageIV<sub>D</sub>. However, for some cases,  
699 where rainfall is dramatically underestimated by the radar system and KGE values are low, IRC-  
700 ICC is shown to provide effective corrections. Otherwise, the IRC-ICC generates physically  
701 constrained corrections spatially (see Figure 10), achieving high KGE values for flood simulations.  
702 Figure 13b shows the histogram of the KGE values across different rainfall products for all events.  
703 Overall, simulated streamflows using MRMS<sub>D</sub> and StageIV<sub>D</sub> exhibit similar hydrologic  
704 performance (the median KGE across events is close to 0.20), on the contrary, post-IRC-ICC  
705 StageIV<sub>D</sub> produce flood simulations with a median KGE above 0.80.

706

#### 707 **4. Discussion and Future Work**

708 Limitations in this study stem mainly from computational constraints rather than  
709 methodology. To quantify the intrinsic uncertainty of the corrected rainfall fields, the IRC-ICC  
710 framework should be applied to each of the members of the ensemble of fractally downscaled  
711 original precipitation fields at each time-step, toward producing an ensemble of corrected  
712 precipitation fields. Because of the high computational costs, the IRC-ICC is applied to the  
713 ensemble mean of the downscaled rainfall fields, which is the product made available as StageIV-  
714 IRC. A default 24-hour duration window is imposed for the implementation of the IRC-ICC,  
715 implying that slow (and deeper) interflow and baseflow contributions to longer lasting floods are  
716 not considered. The current implementation of the IRC-ICC framework was built to support flash  
717 flood studies and only targets shallow subsurface moisture transport, given the critical importance  
718 of shallow soil moisture on the regulation of flood generation and propagation in steep terrain. It

719 is worth noting that for long-lasting rainfall events or regions with relatively flat terrain, slow  
720 interflows would become more important in terms of regulating flood timing, flood volume, and  
721 post IRC-ICC QPE.

722 The IRC results could be further optimized if discharge observations were available with  
723 the same temporal resolution as the model time-step, respectively 15 and 5 minutes in this study.  
724 The IRC-ICC framework could be further advanced through improved model physics and  
725 resolution, utilizing 3D velocity fields to capture the full travel time distributions, and using  
726 alternative approaches to generate IRC ensembles including the deployment of AI tools to test and  
727 calibrate hydrologic models for intercomparison studies, advancing flood forecasting skill, and  
728 support emergency management response. [Liao and Barros \(2023\) generalized IRC results to  
729 quantify uncertainty and developed a generalized precipitation error model using Machine  
730 Learning. In this work, the IRC-ICC framework is applied to the ensemble mean of StageIV  
731 downscaled rainfall. One way to improve the quantification of uncertainty tied to the IRC-ICC  
732 framework would be to apply it to each member of the ensemble of downscaled rainfall fields  
733 separately and then use the distribution of differences among corrected rainfall ensemble members  
734 to quantify uncertainty. The time and computational resources to implement the methodology in this  
735 manner for many watersheds and storms are prohibitive and out of the scope of this work. Nevertheless,  
736 because of the very small area of headwater basins, the differences among ensemble members are expected  
737 to be small \(see also references above\) and thus the variance among ensemble members is small as shown  
738 also in Tao and Barros \(2010\). As we apply the IRC-ICC to larger river basins, this question should be  
739 considered more carefully.](#)

740

Formatted: Font: (Default) Times New Roman

Formatted: Font: (Default) Times New Roman

741 **5. Data Availability Statement**

742 The StageIV-IRC dataset at 250 m 5-minute resolution for 26 basins and 215 events is  
743 available at: <https://doi.org/10.5281/zenodo.14028866>, (Liao and Barros, 2025c), excluding Basin  
744 13 and 14 based on previous discussion. Associated geographic documentation of the selected  
745 basins is also provided via the same link. Initial soil moisture distributions for the studied events  
746 are also available in the same Zenodo repository.

747

748 **6. Conclusion**

749 QPE has been an enduring challenge in hydrology, particularly in complex terrain. Ground-  
750 based radar QPE is plagued with uncertainties from multiple sources, while rain gauge networks  
751 are scarce and suffer from the lack of representativeness in the mountains. To address this grand  
752 challenge, we develop a series of corrections from point-scale to watershed-scale encompassing  
753 event bias, climatology, and water budget closure: the IRC-ICC framework. To our knowledge,  
754 this is the first QPE dataset that meets standard statistical evaluations against point-based  
755 measurements where available and meets water budget closure at flood-event scale, consistent  
756 with nonlinear rainfall-runoff processes in headwater basins, and achieves superior hydrological  
757 performance at sub-hourly.

758 The IRC-ICC framework is successfully adopted in 26 mountainous basins (excluding the  
759 basins that are heavily overlapped with Karst terrain) in the Appalachians for 215 events with  
760 robust success, yielding substantial improvements of streamflow simulation, particularly in terms  
761 of flood volume and timing. The tracking algorithm in the IRC-ICC framework is only updated  
762 when shifting from one hydrological window to another, but not every time step. With enough

Formatted: Font: (Default) Times New Roman, Font color: Custom Color(0,51,204)

Formatted: Font color: Custom Color(0,51,204)

763 computational resources, post-IRC-ICC QPE data should further improve by capturing transient  
764 travel time distributions between model time steps.

765         When using the StageIV-IRC product, flood timing errors are controlled with one hour for  
766 90% of events, compared to less than 20% when using original StageIV, while the median KGE  
767 improved from 0.34 to 0.86 across the events. This change in KGE is achieved by significant  
768 changes in the space-time variance of precipitation that in turn impacts the space-time variability  
769 of rainfall-runoff processes. Results illustrate the importance of initial conditions for less severe  
770 rainfall events, particularly during the beginning of the event, which influences subsequent  
771 streamflow simulations. It should be emphasized that physical parameters are not calibrated for  
772 any precipitation event in any basin in this work. This physics-based IRC-ICC framework can  
773 capture the fundamental physics involved in flash flood events: essentially the fast rainfall-runoff  
774 responses in surface and shallow subsurface layers; therefore, skillful hydrologic prediction is  
775 achieved without model calibration. Instead, the focus is on getting the forcing right.

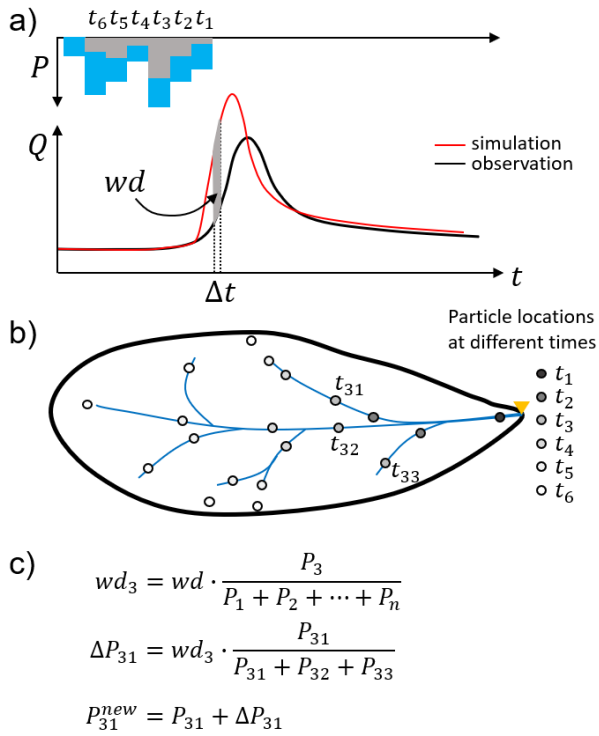
776         The IRC-ICC is a general framework that can be incorporated into any distributed  
777 hydrological model. Thus, the StageIV-IRC dataset also enables meaningful intercomparison  
778 among different radar QPE datasets, providing physics insights into QPE error structure from a  
779 water budget closure perspective, toward improving radar retrievals and to characterize radar-  
780 specific errors related to radar operations at high spatial resolution in the mountains. The  
781 demonstrated success of StageIV-IRC in ungauged basins strongly supports the use of IRC-ICC  
782 in mountainous regions worldwide, where rain gauges are generally not available. Further, this  
783 dataset can be utilized as a reference for building machine learning models (or even deep-learning  
784 models when the number of studied precipitation events is expanded) that can learn the QPE  
785 uncertainties conditional on time of day, weather, climate and geomorphological regimes for both

786 radar QPE analysis and forecasts, advancing the understanding and quantification of orographic  
 787 precipitation uncertainty at high resolution across global mountains.

788 **7. Appendix A**

789 The detailed distribution process of water difference (wd) is illustrated in Figure A1 following  
 790 Section 2.3.8.

791



792

793 **Figure A1** - Schematic depiction of the IRC framework and key mathematical equations. Panel

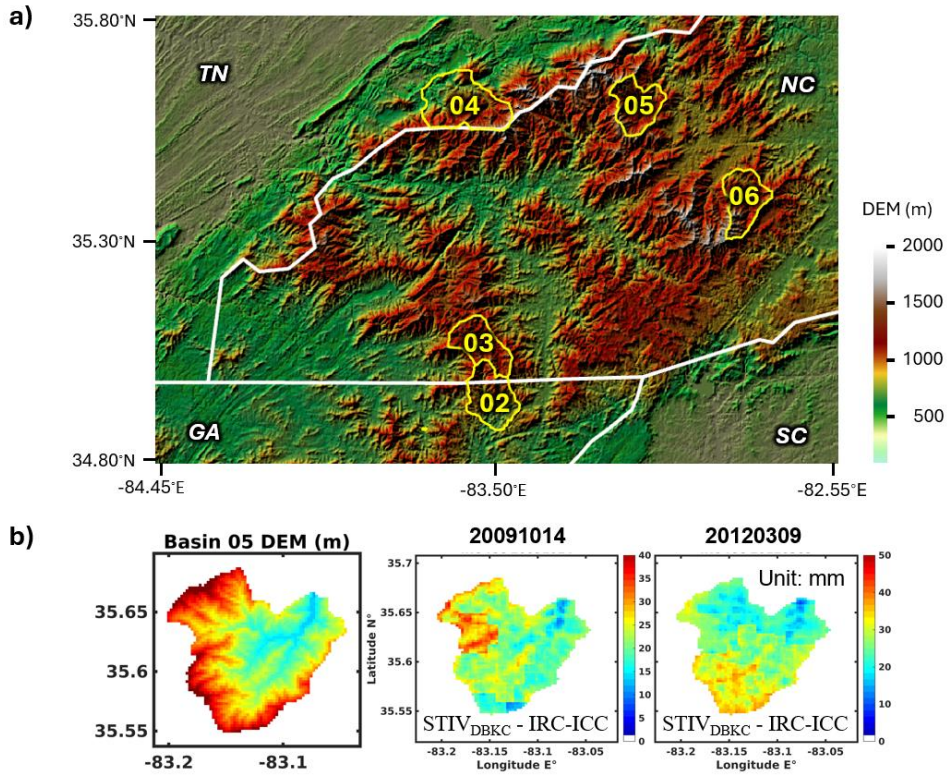
794 (a) illustrates the nonlinear relationship between streamflow and precipitation, where  $wd$

795 represents the residual between discharge simulations and observations at the basin outlet. The  
796 variation of precipitation in the basin as a function of time is shown by the basin hyetograph in  
797 blue. The hyetograph time series (blue) spans the duration of the precipitation event between  $t_1$   
798 to  $t_n$ . In gray is the hyetograph over the area of interest for panels (b) and (c). To map the  
799 streamlines, water particles are launched every time step and their trajectory to the outlet is tracked  
800 and saved. Panel (b) shows the source areas of water particles launched at various time steps  
801 ( $t_1, t_2, \dots, t_6 \dots$ ) from all locations where runoff is produced, and the particles are tracked until they  
802 eventually reach the basin outlet. The streamlines of particles that reach the outlet at the same time  
803 are used to distribute the residuals backwards to the runoff source areas where the particles were  
804 originally launched (e.g., the three particles  $t_{31}, t_{32}$ , and  $t_{33}$  that reach the basin outlet at time  $t_3$ ).  
805 Panel (c) shows the algorithm to calculate the rainfall bias correction at location  $t_{31}$  due to the  
806 residual  $wd_3$  at time  $t_3$ .  $P_1$  is basin averaged rainfall at time  $t_i$ , and  $wd_3$  is the runoff volume to be  
807 corrected at time step  $t_3$ .  $\Delta P_{31}$  is the precipitation correction for pixel  $t_{31}$ , and precipitation  
808 amount at pixel  $t_{31}$  before and after IRC are denoted by  $P_{31}$  and  $P_{31}^{new}$ . This figure is adapted from  
809 Liao and Barros (2025b).

810

811 A zoom in map of the Southern Appalachians is plotted associated with DEM maps of other basins.  
812 A complete set of maps for each individual basin can be requested. Note, the rain gauges used in  
813 this study are plotted in Figure 1, and they are primarily near Basin05.

814



815

816 **Figure A2** – A zoom-in map of the Figure 4 for watersheds in the Southern Appalachians (Panel  
817 a). The DEM map and examples of rainfall event accumulation of Basin 05 (Panel b) to show  
818 rainfall alignment with topography.

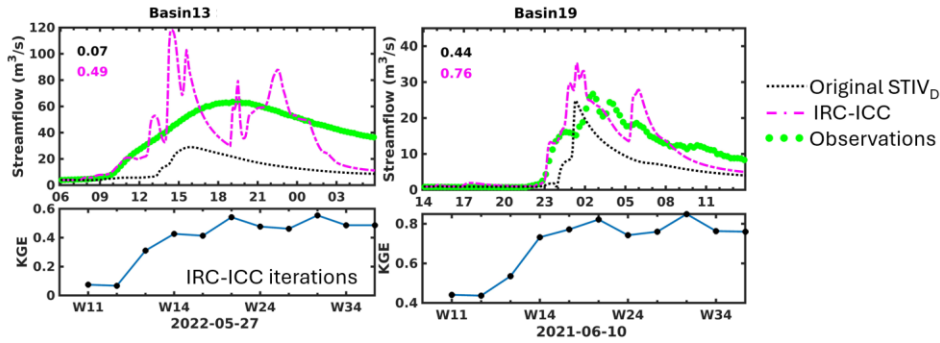
819

820

821

822

823



824

825 **Figure A3** – Examples of the coupled IRC-ICC framework application in Basin 13 and Basin 19  
826 for discussion in the manuscript. KGE values are displayed in the top left corners. Basin 13 is  
827 located in Karst terrain, while the event in Basin 19 is an example with a complex hydrograph.

828

### 829 CREDIT AUTHOR STATEMENT

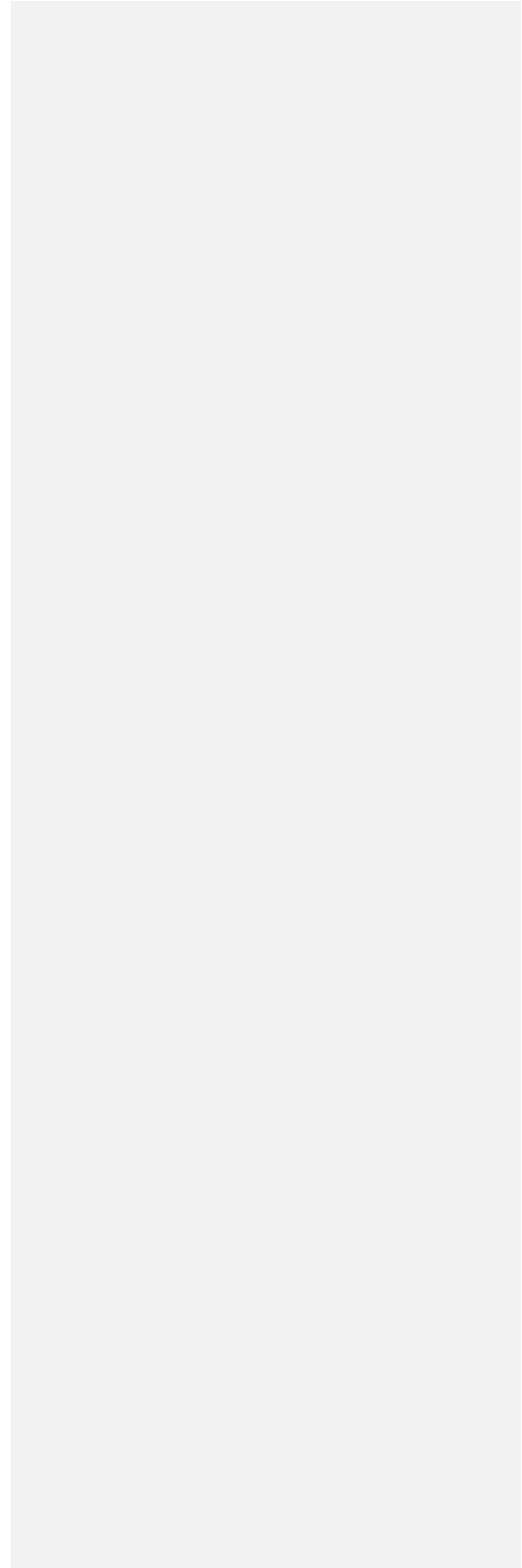
830 M. Liao: Methodology, Data curation, Writing - original draft, Investigation. A. P. Barros:  
831 Conceptualization, Methodology, Writing - review & editing, Supervision, Project administration,  
832 Funding acquisition.

### 833 COMPETING INTERESTS

834 The authors declare there are no competing interests.

### 835 ACKNOWLEDGMENTS

836 The work was supported by NASA Earth System Science Fellowship associated with the first  
837 author and supported by a joint effort from NASA grant 80NSSC19K0685 and a grant from the  
838 IBM [Impact](#) Accelerator program with the second author.



840 **REFERENCES**

- 841 Alimonti, G., Mariani, L., Prodi, F., & Ricci, R. A. (2022). A critical assessment of extreme  
842 events trends in times of global warming. *European Physical Journal - Plus*, 137, 112.  
843 <https://doi.org/10.1140/epjp/s13360-021-02243-9>
- 844 Allen, J. T. (2018). Climate change and severe thunderstorms. In Oxford research encyclopedia  
845 of climate science. <https://doi.org/10.1093/acrefore/9780190228620.013.62>
- 846 Andrieu, H., Creutin, J. D., Delrieu, G., & Faure, D. (1997). Use of a weather radar for the  
847 hydrology of a mountainous area. Part I: Radar measurement interpretation. *Journal of*  
848 *Hydrology*, 193(1-4), 1-25.
- 849 Areerachakul, N., Prongnuch, S., Longsomboon, P., & Kandasamy, J. (2022). Quantitative  
850 precipitation estimation (QPE) rainfall from meteorology radar over Chi Basin. *Hydrology*,  
851 9(10), 178. <https://doi.org/10.3390/hydrology9100178>
- 852 Arulraj, M., & Barros, A. P. (2017). Shallow precipitation detection and classification using  
853 multifrequency radar observations and model simulations. *Journal of Atmospheric and Oceanic*  
854 *Technology*, 34(9), 1963-1983. <https://doi.org/10.1175/JTECH-D-17-0060.1>
- 855 Arulraj, M., & Barros, A. P. (2021). Automatic detection and classification of low-level  
856 orographic precipitation processes from space-borne radars using machine learning. *Remote*  
857 *Sensing of Environment*, 257, 112355. <https://doi.org/10.1016/j.rse.2021.112355>
- 858 Barros, A., & Arulraj, M. (2020). Remote sensing of orographic precipitation. In V. Levizzani,  
859 C. Kidd, D. B. Kirschbaum, C. D. Kummerow, K. Nakamura, & F. J. Turk (Eds.), *Satellite*  
860 *precipitation measurement*. Springer. [https://doi.org/10.1007/978-3-030-35798-6\\_6](https://doi.org/10.1007/978-3-030-35798-6_6)
- 861 Barros, A., Miller, D., Wilson, A., Cutrell, G., Arulraj, M., Super, P., & Petersen, W. (2017).  
862 GPM Ground Validation Southern Appalachian Rain Gauge IPHEX [indicate subset used].  
863 Dataset available online from the NASA Global Hydrometeorology Resource Center DAAC,  
864 Huntsville, Alabama, U.S.A. DOI:  
865 <http://dx.doi.org/10.5067/GPMGV/IPHEX/GAUGES/DATA301>
- 866 Barros, A.P., Petersen, W., Schwaller, M., Cifelli, R., Mahoney, K., Peters-Liddard, C.,  
867 Shepherd, M., Nesbitt, S., Wolff, D., Heymsfield, G. & Starr, D. (2014) NASA GPM-Ground  
868 Validation: Integrated Precipitation and Hydrology Experiment 2014 Science Plan. EPL/Duke  
869 University: Durham, N.C. <https://doi.org/10.7924/G8CC0XMR>.
- 870 Berndt, C., Rabiei, E., & Haberlandt, U. (2014). Geostatistical merging of rain gauge and radar  
871 data for high temporal resolutions and various station density scenarios. *Journal of Hydrology*,  
872 508, 88-101. <https://doi.org/10.1016/j.jhydrol.2013.10.028>
- 873 Bindlish, R. and Barros, A.P., (1996): Aggregation of Digital Terrain Data Using a Modified  
874 Fractal Interpolation Scheme. *Computers & Geosciences*, 22, 907-917.
- 875 Bindlish, R., & Barros, A. P. (2000). Disaggregation of rainfall for one-way coupling of  
876 atmospheric and hydrological models in regions of complex terrain. *Global and Planetary*  
877 *Change*, 25(1-2), 111-132. [https://doi.org/10.1016/S0921-8181\(00\)00024-2](https://doi.org/10.1016/S0921-8181(00)00024-2)
- 878

879 Bohling, G. (2005). Introduction to geostatistics and variogram analysis. *Kansas geological*  
880 *survey*, 1(10), 1-20.

881 Borga, M., Stoffel, M., Marchi, L., Marra, F., & Jakob, M. (2014). Hydrogeomorphic response to  
882 extreme rainfall in headwater systems: Flash floods and debris flows. *Journal of Hydrology*, 518,  
883 194-205.

884 Buytaert, W., Celleri, R., Willems, P., De Bievre, B., & Wyseure, G. (2006). Spatial and  
885 temporal rainfall variability in mountainous areas: A case study from the south Ecuadorian  
886 Andes. *Journal of hydrology*, 329(3-4), 413-421. <https://doi.org/10.1016/j.jhydrol.2006.02.031>

887 Carlson, D., (2010). Influence of lithology on vertical anisotropy of permeability at a field scale  
888 for select Louisiana geologic units. *Gulf Coast Association of Geological Societies Transactions*,  
889 60: 103-118.

890 Cassiraga, E., Gómez-Hernández, J. J., Berenguer, M., Sempere-Torres, D., & Rodrigo-Illarri, J.  
891 (2021). Spatiotemporal precipitation estimation from rain gauges and meteorological radar using  
892 geostatistics. *Mathematical Geosciences*, 53, 499-516. [https://doi.org/10.1007/s11004-020-](https://doi.org/10.1007/s11004-020-09882-1)  
893 [09882-1](https://doi.org/10.1007/s11004-020-09882-1)

894 Chen, J., Kumar, P., 2001. Topographic influence on the seasonal and interannual variation of  
895 water and energy balance of basins in North America. *Journal of Climate*, 14(9).

896 Czigány, S., Pirkhoffer, E., & Geresdi, I. (2010). Impact of extreme rainfall and soil moisture on  
897 flash flood generation. *Quarterly Journal of the Hungarian Meteorological Service*, 114(1-2),  
898 79-100.

899 Deijns, A. A., Dewitte, O., Thiery, W., d'Oreye, N., Malet, J. P., & Kervyn, F. (2022). Timing  
900 landslide and flash flood events from SAR satellite: a regionally applicable methodology  
901 illustrated in African cloud-covered tropical environments. *Natural Hazards and Earth System*  
902 *Sciences*, 22(11), 3679-3700. <https://doi.org/10.5194/nhess-22-3679-2022>

903 Delrieu, G., Wijbrans, A., Boudevillain, B., Faure, D., Bonnifait, L., & Kirstetter, P. E. (2014).  
904 Geostatistical radar-rain gauge merging: A novel method for the quantification of rain estimation  
905 accuracy. *Advances in Water Resources*, 71, 110-124.  
906 <https://doi.org/10.1016/j.advwatres.2014.06.005>

907 Diggle, P. and Ribeiro, P. J., 2007. Model-based geostatistics. Springer Series in Statistics, 230.

908 Dinku, T., Anagnostou, E. N., & Borga, M. (2002). Improving radar-based estimation of rainfall  
909 over complex terrain. *Journal of Applied Meteorology and Climatology*, 41(12), 1163-1178.  
910 [https://doi.org/10.1175/1520-0450\(2002\)041<1163:IRBEOR>2.0.CO;2](https://doi.org/10.1175/1520-0450(2002)041<1163:IRBEOR>2.0.CO;2)

911 Diomede, T., Davolio, S., Marsigli, C., Miglietta, M. M., Moscatello, A., Papetti, P., ... &  
912 Malguzzi, P. (2008). Discharge prediction based on multi-model precipitation forecasts.  
913 *Meteorology and atmospheric physics*, 101, 245-265. <https://doi.org/10.1007/s00703-007-0285-0>

914 Dobler, C., Hagemann, S., Wilby, R. L., & Stötter, J. (2012). Quantifying different sources of  
915 uncertainty in hydrological projections in an Alpine watershed. *Hydrology and Earth System*  
916 *Sciences*, 16(11), 4343-4360. <https://doi.org/10.5194/hess-16-4343-2012>

917 Duan, Y., & Barros, A. P. (2017). Understanding how low-level clouds and fog modify the  
918 diurnal cycle of orographic precipitation using in situ and satellite observations. *Remote*  
919 *Sensing*, 9(9), 920. <https://doi.org/10.3390/rs9090920>

- 920 Durden, S. L., Haddad, Z. S., Kitiyakara, A., & Li, F. K. (1998). Effects of nonuniform beam  
921 filling on rainfall retrieval for the TRMM precipitation radar. *Journal of Atmospheric and*  
922 *Oceanic Technology*, 15(3), 635-646. [https://doi.org/10.1175/1520-  
923 0426\(1998\)015<0635:EONBFO>2.0.CO;2](https://doi.org/10.1175/1520-0426(1998)015<0635:EONBFO>2.0.CO;2)
- 924 Foresti, L., & Pozdnoukhov, A. (2012). Exploration of alpine orographic precipitation patterns  
925 with radar image processing and clustering techniques. *Meteorological Applications*, 19(4), 407-  
926 419. <https://doi.org/10.1002/met.272>
- 927 Freeze, R.A., Cherry, J.A., 1979. *Groundwater*. Englewood Cliffs, N.J. : Prentice-Hall.
- 928 Fulton, J., & Ostrowski, J. (1998). Measuring real-time streamflow using emerging technologies:  
929 Radar, hydroacoustics, and the probability concept. *Journal of Hydrology*, 357(1-2), 1-10.  
930 <https://doi.org/10.1016/j.jhydrol.2008.03.028>
- 931 Gentilucci, M., Bufalini, M., D'Aprile, F., Materazzi, M., & Pambianchi, G. (2021). Comparison  
932 of data from rain gauges and the IMERG product to analyse precipitation in mountain areas of  
933 central Italy. *ISPRS International Journal of Geo-Information*, 10(12), 795.  
934 <https://doi.org/10.3390/ijgi10120795>
- 935 Goudenhoofd, E., & Delobbe, L. (2009). Evaluation of radar-gauge merging methods for  
936 quantitative precipitation estimates. *Hydrology and Earth System Sciences*, 13(2), 195-203.  
937 <https://doi.org/10.5194/hess-13-195-2009>
- 938 Grillakis, M. G., Koutroulis, A. G., Komma, J., Tsanis, I. K., Wagner, W., & Blöschl, G. (2016).  
939 Initial soil moisture effects on flash flood generation—A comparison between basins of  
940 contrasting hydro-climatic conditions. *Journal of Hydrology*, 541, 206-217.
- 941 Gupta, H. V., Kling, H., Yilmaz, K. K., & Martinez, G. F. (2009). Decomposition of the mean  
942 squared error and NSE performance criteria: Implications for improving hydrological  
943 modelling. *Journal of hydrology*, 377(1-2), 80-91. <https://doi.org/10.1016/j.jhydrol.2009.08.003>
- 944 Gupta, V., Nautiyal, H., Kumar, V., Jamir, I., & Tandon, R. S. (2016). Landslide hazards around  
945 Uttarkashi township, Garhwal Himalaya, after the tragic flash flood in June 2013. *Natural*  
946 *Hazards*, 80, 1689-1707. <https://doi.org/10.1007/s11069-015-2048-4>
- 947 Harrison, D. L., Driscoll, S. J., & Kitchen, M. (2000). Improving precipitation estimates from  
948 weather radar using quality control and correction techniques. *Meteorological Applications*, 7(2),  
949 135-144. <https://doi.org/10.1017/S1350482700001468>
- 950 Huffman, G. J., R. F. Adler, D. T. Bolvin, G. J. Gu, E. J. Nelkin, K. P. Bowman, Y. Hong, E. F.  
951 Stocker, and D. B. Wolff (2007), The TRMM multisatellite precipitation analysis (TMPA):  
952 Quasi-global, multiyear, combined-sensor precipitation estimates at fine scales, *J.*  
953 *Hydrometeorol.*, 8(1), 38–55. <https://doi.org/10.1175/JHM560.1>
- 954 Iwasaki, K., Katsuyama, M., & Tani, M. (2020). Factors affecting dominant peak-flow runoff-  
955 generation mechanisms among five neighbouring granitic headwater catchments. *Hydrological*  
956 *Processes*, 34(5), 1154-1166. <https://doi.org/10.1002/hyp.13656>
- 957 Kim, G., & Barros, A. P. (2001). Quantitative flood forecasting using multisensor data and  
958 neural networks. *Journal of Hydrology*, 246(1-4), 45-62. [https://doi.org/10.1016/S0022-  
959 1694\(01\)00353-5](https://doi.org/10.1016/S0022-1694(01)00353-5)

Field Code Changed

Field Code Changed

960 Kobold, M., & Sušelj, K. (2005). Precipitation forecasts and their uncertainty as input into  
961 hydrological models. *Hydrology and Earth System Sciences*, 9(4), 322-332.  
962 <https://doi.org/10.5194/hess-9-322-2005>

963 Kochendorfer, J., Rasmussen, R., Wolff, M., Baker, B., Hall, M. E., Meyers, T., ... & Leeper, R.  
964 (2017). The quantification and correction of wind-induced precipitation measurement errors.  
965 *Hydrology and Earth System Sciences*, 21(4), 1973-1989. [https://doi.org/10.5194/hess-21-1973-](https://doi.org/10.5194/hess-21-1973-2017)  
966 [2017](https://doi.org/10.5194/hess-21-1973-2017)

967 Komma, J., Reszler, C., Blöschl, G., & Haiden, T. (2007). Ensemble prediction of floods–  
968 catchment non-linearity and forecast probabilities. *Natural Hazards and Earth System Sciences*,  
969 7(4), 431-444.

970 Konrad II, C. E. (1994). Moisture trajectories associated with heavy rainfall in the Appalachian  
971 region of the United States. *Physical Geography*, 15(3), 227-248.  
972 <https://doi.org/10.1080/02723646.1994.10642514>

973 Kreklow, J., Tetzlaff, B., Burkhard, B., & Kuhnt, G. (2020). Radar-based precipitation  
974 climatology in Germany—developments, uncertainties and potentials. *Atmosphere*, 11(2), 217.  
975 <https://doi.org/10.3390/atmos11020217>

976 Laiolo, P., Gabellani, S., Campo, L., Silvestro, F., Delogu, F., Rudari, R., ... & Puca, S. (2016).  
977 Impact of different satellite soil moisture products on the predictions of a continuous distributed  
978 hydrological model. *International Journal of Applied Earth Observation and Geoinformation*,  
979 48, 131-145. <https://doi.org/10.1016/j.jag.2015.06.002>

980 Li, J., & Heap, A. D. 2008. A review of spatial interpolation methods for environmental  
981 scientists. 11-12.

982 Liao, M., & Barros, A. P. (2019). The Integrated Precipitation and Hydrology Experiment-  
983 Hydrologic Applications for the Southeast US (IPHEX-H4SE) Part IV: High-Resolution  
984 Enhanced Stage IV-Rain gauge Combined Precipitation Product [Dataset]. Durham, NC: Duke  
985 Digital Repository. <https://idn.duke.edu/ark:/87924/r4pc2zd75>

986 Liao, M., & Barros, A. P. (2022). Toward optimal rainfall – Hydrologic QPE correction in  
987 headwater basins. *Remote Sensing of Environment*, 279, 113107.  
988 <https://doi.org/10.1016/j.rse.2022.113107>

989 Liao, M., & Barros, A.P., (2025a). Model Celerity-Discharge Behavior in Complex Terrain to  
990 Improve Orographic Quantitative Precipitation Estimation and Hydrologic Prediction in  
991 Headwater Basins. *Water Resources Research*, <https://doi.org/10.1029/2024WR038446>

992 Liao, M., & Barros, A.P., (2025b). Toward optimal rainfall – Hydrologic QPE Correction in  
993 Headwater Basins — Closing the Water Budget within Observational Uncertainty Through  
994 Correcting Initial Soil Moisture Conditions. *J. Hydrology-Reg. Studies*,  
995 <https://doi.org/10.1016/j.ejrh.2025.102700>.

996 Liao, M., & Barros, A. (2025c). StageIV-IRC – A High-resolution Dataset of Extreme  
997 Orographic Quantitative Precipitation Estimates (QPE) Constrained to Water Budget Closure for  
998 Historical Floods in the Appalachian Mountains [Data set]. Zenodo.  
999 <https://doi.org/10.5281/zenodo.14028866>

1000

Field Code Changed

Formatted: Portuguese (Brazil)

Field Code Changed

1001 Lin, Y., & Mitchell, K. E. (2005), The NCEP stage II/IV hourly precipitation analyses:  
 1002 Development and applications, paper presented at 19th Conference on Hydrology [Dataset], Am.  
 1003 Meteorol. Soc., San Diego, Calif., 9–13 Jan.

1004 Linsley, R.K., Kohler, J., Max A., Paulhus, J.L.H., (1982). Hydrology for Engineers. Water  
 1005 Resources and Environmental Engineering. McGraw-Hill, New York.

1006 Lumbroso, D., & Gaume, E. (2012). Reducing the uncertainty in indirect estimates of extreme  
 1007 flash flood discharges. *Journal of hydrology*, 414, 16-30.

1008 Maggioni, V., & Massari, C. (2018). On the performance of satellite precipitation products in  
 1009 riverine flood modeling: A review. *Journal of hydrology*, 558, 214-224.

1010 Marchi, L., Borga, M., Preciso, E., & Gaume, E. (2010). Characterization of selected extreme  
 1011 flash floods in Europe and implications for flood risk management. *Journal of Hydrology*, 394(1-  
 1012 2), 118-133.

1013 McBratney, A. B., & Webster, R. (1986). Choosing functions for semi-variograms of soil  
 1014 properties and fitting them to sampling estimates. *Journal of soil Science*, 37(4), 617-639.

1015 McBride, J. L., & Ebert, E. E. (2000). Verification of quantitative precipitation forecasts from  
 1016 operational numerical weather prediction models over Australia. *Weather and Forecasting*,  
 1017 15(1), 103-121.

1018 McKee, J. L., & Binns, A. D. (2016). A review of gauge–radar merging methods for quantitative  
 1019 precipitation estimation in hydrology. *Canadian Water Resources Journal/Revue canadienne des*  
 1020 *ressources hydriques*, 41(1-2), 186-203. <https://doi.org/10.1080/07011784.2015.1064786>

1021 Milly, P. C. D., Wetherald, R. T., Dunne, K. A., & Delworth, T. L. (2002). Increasing risk of  
 1022 great floods in a changing climate. *Nature*, 415(6871), 514-517. <https://doi.org/10.1038/415514a>

1023 Mockler, E. M., Chun, K. P., Sapriza-Azuri, G., Bruen, M., & Wheeler, H. S. (2016). Assessing  
 1024 the relative importance of parameter and forcing uncertainty and their interactions in conceptual  
 1025 hydrological model simulations. *Advances in Water Resources*, 97, 299-313.  
 1026 <https://doi.org/10.1016/j.advwatres.2016.10.008>

1027 Mtibaa, S., & Asano, S. (2022). Hydrological evaluation of radar and satellite gauge-merged  
 1028 precipitation datasets using the SWAT model: Case of the Terauchi catchment in Japan. *Journal*  
 1029 *of Hydrology: Regional Studies*, 42, 101134. <https://doi.org/10.1016/j.ejrh.2022.101134>

1030 Nanding, N., Rico-Ramirez, M. A., & Han, D. (2015). Comparison of different radar-rain gauge  
 1031 rainfall merging techniques. *Journal of Hydroinformatics*, 17(3), 422-445.  
 1032 <https://doi.org/10.2166/hydro.2015.001>

1033 Nogueira, M., and Barros, A.P., (2015): Transient Stochastic Downscaling of Quantitative  
 1034 Precipitation Estimates for Hydrological Applications. *J. Hydrology*, No. 529, 1407- [1421](https://doi.org/10.1016/j.jhydrol.2015.08.041).  
 1035 <https://doi.org/10.1016/j.jhydrol.2015.08.041>.

1036 Oliver, M. A., & Webster, R. (2015). *Basic steps in geostatistics: the variogram and kriging*  
 1037 (Vol. 106). Cham, Switzerland: Springer International Publishing.

1038 Penna, D., Tromp-van Meerveld, H. J., Gobbi, A., Borga, M., & Dalla Fontana, G. (2011). The  
 1039 influence of soil moisture on threshold runoff generation processes in an alpine headwater

1040 catchment. *Hydrology and Earth System Sciences*, 15(3), 689-702. [https://doi.org/10.5194/hess-](https://doi.org/10.5194/hess-15-689-2011)  
1041 [15-689-2011](https://doi.org/10.5194/hess-15-689-2011)

1042 Pielke, R. A., & Downton, M. W. (2000). Precipitation and damaging floods: Trends in the  
1043 United States, 1932–97. *Journal of climate*, 13(20), 3625-3637. [https://doi.org/10.1175/1520-](https://doi.org/10.1175/1520-0442(2000)013<3625:PADFTI>2.0.CO;2)  
1044 [0442\(2000\)013<3625:PADFTI>2.0.CO;2](https://doi.org/10.1175/1520-0442(2000)013<3625:PADFTI>2.0.CO;2)

1045 Prat, O. P., & Barros, A. P. (2010a). Assessing satellite-based precipitation estimates in the  
1046 Southern Appalachian mountains using rain gauges and TRMM PR. *Advances in*  
1047 *Geosciences*, 25, 143-153. <https://doi.org/10.5194/adgeo-25-143-2010>

1048 Prat, O. P., & Barros, A. P. (2010b). Ground observations to characterize the spatial gradients  
1049 and vertical structure of orographic precipitation—Experiments in the inner region of the Great  
1050 Smoky Mountains. *Journal of Hydrology*, 391(1-2), 141-156.  
1051 <https://doi.org/10.1016/j.jhydrol.2010.07.013>

1052 Rafiecinasab, A., Norouzi, A., Seo, D. J., & Nelson, B. (2015). Improving high-resolution  
1053 quantitative precipitation estimation via fusion of multiple radar-based precipitation products.  
1054 *Journal of Hydrology*, 531, 320-336. <https://doi.org/10.1016/j.jhydrol.2015.04.066>

1055 Schiemann, R., Erdin, R., Willi, M., Frei, C., Berenguer, M., & Sempere-Torres, D. (2011).  
1056 Geostatistical radar-rain gauge combination with nonparametric correlograms: methodological  
1057 considerations and application in Switzerland. *Hydrology and Earth System Sciences*, 15(5),  
1058 1515-1536. <https://doi.org/10.5194/hess-15-1515-2011>

1059 Schumacher, R. S. (2017). Heavy rainfall and flash flooding. In *Oxford research encyclopedia of*  
1060 *natural hazard science*. <https://doi.org/10.1093/acrefore/9780199389407.013.132>

1061 Shao, Y., Fu, A., Zhao, J., Xu, J., & Wu, J. (2021). Improving quantitative precipitation  
1062 estimates by radar-rain gauge merging and an integration algorithm in the Yishu River  
1063 catchment, China. *Theoretical and Applied Climatology*, 144, 611-623.  
1064 <https://doi.org/10.1007/s00704-021-03526-y>

1065 Sideris, I. V., Gabella, M., Erdin, R., & Germann, U. (2013). Real-time radar–rain-gauge  
1066 merging using spatio-temporal co-kriging with external drift in the alpine terrain of Switzerland.  
1067 *Quarterly Journal of the Royal Meteorological Society*, 140(680), 1097-1111.  
1068 <https://doi.org/10.1002/qj.2188>

1069 Silvestro, F., Rossi, L., Campo, L., Parodi, A., Fiori, E., Rudari, R., & Ferraris, L. (2019).  
1070 Impact-based flash-flood forecasting system: Sensitivity to high resolution numerical weather  
1071 prediction systems and soil moisture. *Journal of Hydrology*, 572, 388-402.  
1072 <https://doi.org/10.1016/j.jhydrol.2019.02.055>

1073 Smith, J. A., Baeck, M. L., Ntelekos, A. A., Villarini, G., & Steiner, M. (2011). Extreme rainfall  
1074 and flooding from orographic thunderstorms in the central Appalachians. *Water Resources*  
1075 *Research*, 47(4). <https://doi.org/10.1029/2010WR010190>

1076 Špitalar, M., Gourley, J. J., Lutoff, C., Kirstetter, P. E., Brilly, M., & Carr, N. (2014). Analysis of  
1077 flash flood parameters and human impacts in the US from 2006 to 2012. *Journal of hydrology*,  
1078 519, 863-870. Tao, K., and Barros, A.P., 2010: Fractal Downscaling of Satellite Precipitation  
1079 Products for Hydrometeorological Applications. *J. Atmos. Oceanic Technol.*, 27 (3), 409-427.  
1080 <https://doi.org/10.1175/2009JTECHA1219.1>

1081 Tao, K., & Barros, A. P. (2010). Using fractal downscaling of satellite precipitation products for  
1082 hydrometeorological applications. *Journal of Atmospheric and Oceanic Technology*, 27(3), 409-  
1083 427.

1084 Tao, J., & Barros, A. P. (2013). Prospects for flash flood forecasting in mountainous regions—An  
1085 investigation of Tropical Storm Fay in the Southern Appalachians. *Journal of Hydrology*, 506,  
1086 69-89. <https://doi.org/10.1016/j.jhydrol.2013.02.052>

1087 Tao, J., & Barros, A. P. (2014). Coupled prediction of flood response and debris flow initiation  
1088 during warm-and cold-season events in the Southern Appalachians, USA. *Hydrology and Earth  
1089 System Sciences*, 18(1), 367-388. <https://doi.org/10.5194/hess-18-367-2014>

1090 Tao, J., Wu, D., Gourley, J., Zhang, S. Q., Crow, W., Peters-Lidard, C., & Barros, A. P. (2016).  
1091 Operational hydrological forecasting during the IPHEX-IOP campaign—Meet the  
1092 challenge. *Journal of hydrology*, 541, 434-456. <https://doi.org/10.1016/j.jhydrol.2016.02.019>

1093 Tao, J., & Barros, A. P. (2018). Multi-year atmospheric forcing datasets for hydrologic modeling  
1094 in regions of complex terrain—Methodology and evaluation over the Integrated Precipitation and  
1095 Hydrology Experiment 2014 domain. *Journal of Hydrology*, 567, 824-842.  
1096 <https://doi.org/10.1016/j.jhydrol.2016.12.058>

1097 Tao, J., and Barros, A.P., 2019: Multi-Year Surface Radiative Properties and Vegetation  
1098 Parameters for Hydrologic Modeling in Regions of Complex Terrain – Methodology and  
1099 Evaluation over the IPHEX2014 Domain. *J. Hydrology-Reg. Studies*, 22, e100596. <https://doi.org/10.1016/j.ejrh.2019.100596>.

1101 Troch, P. A., Smith, J. A., Wood, E. F., & de Troch, F. P. (1994). Hydrologic controls of large  
1102 floods in a small basin: central Appalachian case study. *Journal of Hydrology*, 156(1-4), 285-  
1103 309. [https://doi.org/10.1016/0022-1694\(94\)90082-5](https://doi.org/10.1016/0022-1694(94)90082-5)

1104 Uber, M., Vandervaere, J. P., Zin, I., Braud, I., Heistermann, M., Legoût, C., ... & Nord, G.  
1105 (2018). How does initial soil moisture influence the hydrological response? A case study from  
1106 southern France. *Hydrology and Earth System Sciences*, 22(12), 6127-6146.  
1107 <https://doi.org/10.5194/hess-22-6127-2018>

1108 Vignal, B., Galli, G., Joss, J., & Germann, U. (2000). Three methods to determine profiles of  
1109 reflectivity from volumetric radar data to correct precipitation estimates. *Journal of Applied  
1110 Meteorology and Climatology*, 39(10), 1715-1726. <https://doi.org/10.1175/1520-0450-39.10.1715>

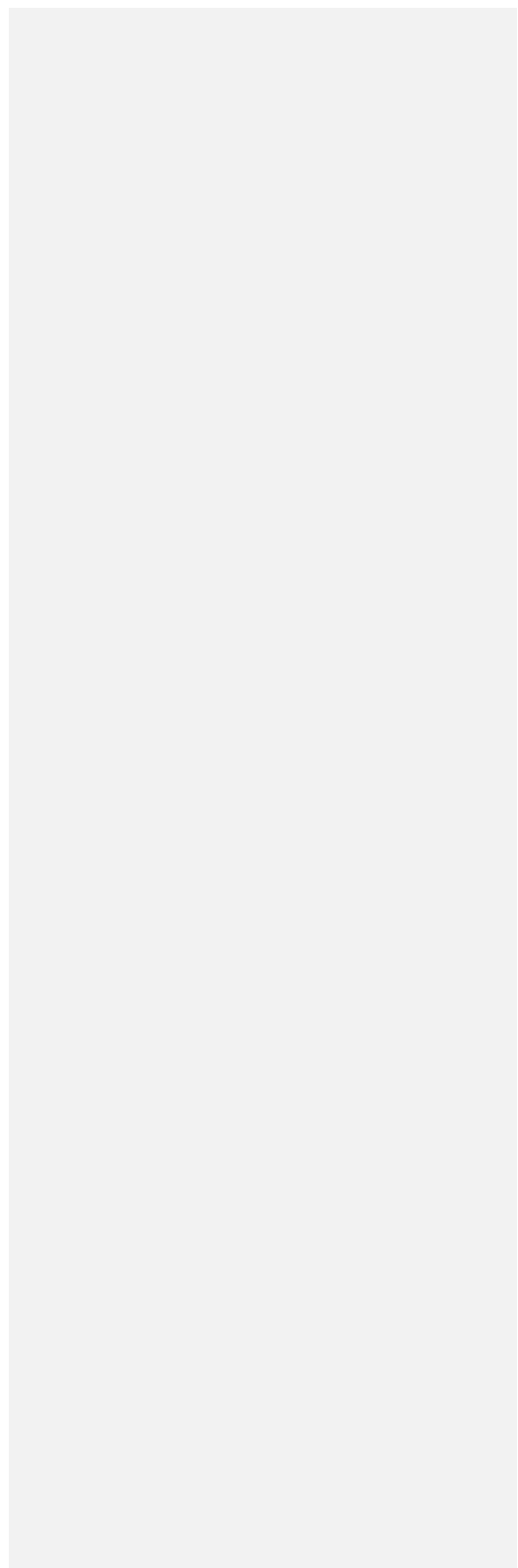
1112 Villarini, G., & Krajewski, W. F. (2010). Review of the different sources of uncertainty in single  
1113 polarization radar-based estimates of rainfall. *Surveys in geophysics*, 31, 107-129.  
1114 <https://doi.org/10.1007/s10712-009-9079-x>

1115 Vivoni, E. R., Entekhabi, D., Bras, R. L., & Ivanov, V. Y. (2007). Controls on runoff generation  
1116 and scale-dependence in a distributed hydrologic model. *Hydrology and Earth System Sciences*,  
1117 11(5), 1683-1701. <https://doi.org/10.5194/hess-11-1683-2007>

1118 Wang, K. H., Chu, T., Yang, M. D., & Chen, M. C. (2020). Geostatistical based models for the  
1119 spatial adjustment of radar rainfall data in typhoon events at a high-elevation river watershed.  
1120 *Remote Sensing*, 12(9), 1427. <https://doi.org/10.3390/rs12091427>

- 1121 Wang, J., & Wolff, D. B. (2010). Evaluation of TRMM ground-validation radar-rain errors using  
1122 rain gauge measurements. *Journal of Applied Meteorology and Climatology*, 49(2), 310-324.
- 1123 Weiland, F. C. S., Vrugt, J. A., Weerts, A. H., & Bierkens, M. F. (2015). Significant uncertainty  
1124 in global scale hydrological modeling from precipitation data errors. *Journal of Hydrology*, 529,  
1125 1095-1115. <https://doi.org/10.1016/j.jhydrol.2015.08.061>
- 1126 Wehbe, Y., Temimi, M., & Adler, R. F. (2020). Enhancing precipitation estimates through the  
1127 fusion of weather radar, satellite retrievals, and surface parameters. *Remote Sensing*, 12(8), 1342.  
1128 <https://doi.org/10.3390/rs12081342>
- 1129 Wernberg, T., Smale, D., Tuya, F., Thomsen, M. S., Langlois, T. J., de Bettignies, T., Bennett,  
1130 S., & Rousseaux, C. S. (2013). An extreme climatic event alters marine ecosystem structure in a  
1131 global biodiversity hotspot. *Nature Climate Change*, 3, 78–82.  
1132 <https://doi.org/10.1038/nclimate1627>
- 1133 Wilson, A. M., & Barros, A. P. (2014). An investigation of warm rainfall microphysics in the  
1134 southern Appalachians: Orographic enhancement via low-level seeder–feeder  
1135 interactions. *Journal of the Atmospheric Sciences*, 71(5), 1783-1805.  
1136 <https://doi.org/10.1175/JAS-D-13-0228.1>
- 1137 Wolvin, S., Strong, C., Rupper, S., & Steenburgh, W. J. (2024). Climatology of orographic  
1138 precipitation gradients over High Mountain Asia derived from dynamical downscaling. *Journal*  
1139 *of Geophysical Research: Atmospheres*, 129(20), e2024JD041010.  
1140 <https://doi.org/10.1029/2024JD041010>
- 1141 Yildiz, O., & Barros, A. P. (2004). Climate variability, water resources, and hydrologic  
1142 extremes—Modeling the water and energy budgets. In *Climate and Hydrology in Mountain*  
1143 *Areas*, (Eds. C. de Jong, D. Collins, and R. Ranzi), John Wiley and Sons (Pub.) , 303-318.  
1144 <https://doi.org/10.1002/0470858249.ch20>
- 1145 Yildiz, O., & Barros, A. P. (2007). Elucidating vegetation controls on the hydroclimatology of a  
1146 mid-latitude basin. *Journal of Hydrology*, 333(2-4), 431-448.  
1147 <https://doi.org/10.1016/j.jhydrol.2006.09.010>
- 1148 Yıldız, O., & Barros, A. P. (2009). Evaluating spatial variability and scale effects on hydrologic  
1149 processes in a midsize river basin. *Sci. Res. Essays*, 4, 217-225.  
1150 <https://doi.org/10.5897/SRE.9000465>
- 1151 Zappa, M., Jaun, S., Germann, U., Walser, A., & Fundel, F. (2011). Superposition of three  
1152 sources of uncertainties in operational flood forecasting chains. *Atmospheric Research*, 100(2-3),  
1153 246-262. <https://doi.org/10.1016/j.atmosres.2010.12.005>
- 1154 Zehe, E., & Blöschl, G. (2004). Predictability of hydrologic response at the plot and catchment  
1155 scales: Role of initial conditions. *Water Resources Research*, 40(10).
- 1156 Zhang, J., Howard, K., Langston, C., Kaney, B., Qi, Y., Tang, L., Grams, H., Wang, Y., Cocks,  
1157 S., Martinaitis, S., Arthur, A., Cooper, K., Brogden, J., & Kitzmiller, D. (2016). Multi-radar  
1158 multi-sensor (MRMS) quantitative precipitation estimation: Initial operating capabilities  
1159 [Dataset]. *Bulletin of the American Meteorological Society*, 97(4), 621–638.  
1160 <https://doi.org/10.1175/BAMS-D-14-00174.1>

- 1161 Zhang, X., & Anagnostou, E. N. (2019). Evaluation of numerical weather model-based satellite  
1162 precipitation adjustment in tropical mountainous regions. *Journal of Hydrometeorology*, 20(3),  
1163 431-445. <https://doi.org/10.1175/JHM-D-18-0008.1>
- 1164 Zhang, Y., Schaap, M. G., & Zha, Y. (2018). A high-resolution global map of soil hydraulic  
1165 properties produced by a hierarchical parameterization of a physically based water retention  
1166 model. *Water Resources Research*, 54(12), 9774-9790. <https://doi.org/10.1029/2018WR023539>
- 1167 Zimmerman, D. L., & Zimmerman, M. B. (1991). A comparison of spatial semivariogram  
1168 estimators and corresponding ordinary kriging predictors. *Technometrics*, 33(1), 77-91.  
1169 <https://doi.org/10.1080/00401706.1991.10484771>
- 1170
- 1171



1173 **LIST OF TABLES**

1174 **Table 1** - Raingauge index and exact locations as illustrated in Figure 1. Two rain gauges  
1175 highlighted in bold font are installed at Purchase Knob, a supersite in the inner mountain region.  
1176 Locations equipped with more than one raingauge (collocated) are shaded in grey color, and these  
1177 collocated raingauges generally differ in tipping sizes. This table is adapted from Liao and Barros  
1178 (2019).

1179 **Table 2** - Hydrologic skills used in this work.

1180 **Table 3** - Information table for selected basins and corresponding streamflow gauges used in this  
1181 work. This table is adapted from Liao and Barros (2025b).

1182

1183

1184

1185

1186 **Table 1** – Raingauge index and exact locations as illustrated in Figure 1. Two rain gauges  
 1187 highlighted in bold font are installed at Purchase Knob, a supersite in the inner mountain region.  
 1188 Locations equipped with more than one raingauge (collocated) are shaded in grey color, and these  
 1189 collocated raingauges generally differ in tipping sizes. This table is adapted from Liao and Barros  
 1190 (2019).

NO.	Site ID.	Latitude	Longitude	Elevation (m)
01	RG 001	35.398	-82.913	1156
02	RG 002	35.417	-82.971	1731
03	RG 003	35.384	-82.916	1609
04	RG 004	35.368	-82.990	1922
05	RG 005	35.408	-82.964	1520
06	RG 008	35.382	-82.973	1737
07	RG 010	35.456	-82.946	1478
08	RG 100	35.586	-83.072	1495
09	RG 100T	35.587	-83.064	1485
10	RG 101	35.575	-83.088	1520
11	RG 102	35.563	-83.103	1635
12	RG 103	35.553	-83.117	1688
13	RG 104	35.554	-83.088	1584
14	RG 106	35.432	-83.029	1210
15	RG 109	35.495	-83.040	1500
16	RG 110	35.548	-83.148	1563
17	RG 300	35.726	-83.216	1558
18	RG 301	35.705	-83.255	2003
19	RG 302	35.721	-83.246	1860
<b>20</b>	<b>RG 303PK</b>	<b>35.586</b>	<b>-83.072</b>	<b>1495</b>
<b>21</b>	<b>RG 303S</b>	<b>35.762</b>	<b>-83.162</b>	<b>1490</b>
22	RG 304	35.670	-83.182	1820
23	RG 305	35.691	-83.131	1630
24	RG 306	35.745	-83.171	1536
25	RG 307	35.651	-83.199	1624
26	RG 308	35.730	-83.182	1471
27	RG 309	35.682	-83.150	1604
28	RG 310	35.702	-83.122	1756
29	RG 311	35.765	-83.140	1036
30	RG 400	35.702	-83.122	1756
31	RG 401	35.651	-83.199	1624
32	RG 402	35.721	-83.246	1860
33	RG 403	35.517	-83.101	925
34	RG 407	35.517	-83.101	925

1191

1192

1193 **Table 2:** Hydrologic skills used in this work.

Notation	Information	Reference
KGE	Kling-Gupta efficiency	Eq. (19) /Gupta et al. (2009)
EV	Relative error in flood volume	Eq. (20)
EPT	Error in peak flow timing	Flood front timing differences
EPV	Relative Error in maximum flow rate	Eq. (21)

1194

1195 **Table 3** – Information table for selected basins and corresponding streamflow gauges used in this  
 1196 work. This table is adapted from Liao and Barros (2025b).

Basin index	USGS Gauge ID	Drainage area (km <sup>2</sup> )	Basin highest elevation (m)	Basin relief (m)	Location
1	3544970	118.7	1442	847	GA
2	2178400	176.1	1629	1051	GA
3	3504000	149.9	1667	1032	NC
4	3497300	317.6	1999	1651	TN
5	3460000	148.1	1879	1174	NC
6	3456500	152.8	1873	1157	NC
8	344894205	41.3	1995	1221	NC
9	3463300	134.3	1989	1425	NC
10	3400500	234.7	1257	1257	KY
11	3479000	283.3	1772	1216	NC
13	3182700	447.3	1111	717	WV
14	2011460	194.4	1388	763	VA
15	1620500	54.5	1321	712	VA
16	3180500	426.8	1416	621	WV
17	3068800	437.1	1471	908	WV
18	1595000	234.8	1230	560	MD
19	1595300	130.3	1069	712	WV
20	1544500	445.9	765	457	PA
21	1422747	81.4	766	394	NY
22	1415000	106.8	1019	636	NY
23	1413398	152.8	1094	754	NY
24	13621955	41.7	1074	717	NY
25	1421610	51.3	970	497	NY
26	1074520	389.4	1582	1582	NH
27	10642505	294.9	1895	1693	NH
28	1137500	300.3	1894	1546	NH
29	1133000	183.2	975	719	VT
30	1055000	334.1	1143	975	MAINE

1197

1198

1199 **LIST OF FIGURES**

1200 **Figure 1** - Map of IPHEX (Barros et al., 2014) ground-based observations in the Southern  
1201 Appalachians. Each rain gauge is denoted as a character string starting with three-digit number  
1202 potentially followed by extra letters; locations started with a letter P represent disdrometers. The  
1203 basic information regarding these stations is available in Table 1. This figure is adapted from Liao  
1204 and Barros (2019).

1205 **Figure 2** – Workflow to generate the product  $STIV_{DBKC}$ .

1206 **Figure 3** – An illustration of the structure of IRC, ICC and the coupled IRC-ICC framework  
1207 including **a)** the residual hydrograph between the observed and simulated discharge, with the  
1208 discharge water difference  $wd(t)$  being distributed across the time window  $T$ ; **b)** Example of travel  
1209 time distribution  $TT(t)$  and map (inset) illustrating a hypothetical distribution of runoff source  
1210 areas (in red,  $ns=3$ ) with travel time  $x_2$  contributing to streamflow at time  $t$ , meaning that at time  
1211  $t-x_2$  there are three pixels ( $ns=3$ ) generating runoff that reaches the outlet at time  $t$ .  $T$  is the time  
1212 window over which runoff source areas with  $TT < T$  are mapped and the inverse rainfall correction  
1213 (IRC) are applied; **c)** Example of IRC windows guided by timescales of dominant hydrological  
1214 processes. The first window solely covers the initial streamflow conditions before the target event.  
1215 The second window depicts the early rising limb of the hydrograph. The third window captures  
1216 the steep rising limb of the hydrograph until it reaches the peak flow. The fourth and fifth windows  
1217 correspond to interflow-dominant and baseflow-dominant stages of the recession curve  
1218 respectively, separated by the recession inflection point; **d)** A schematic drawing that shows  
1219 different characteristic timings in a hydrograph with the implementation of the Initial Condition  
1220 Correction (ICC) strategy. Specifically,  $T_{r^*}$  and  $T_r$  represent the timing of flood front in simulations  
1221 and observations, respectively.  $T_p$  is the timing of observed maximum flood. The inflection point  
1222 of the recession curve of the observations is denoted as  $T_i$ . Flow differences at  $t_1$  and  $t_2$  are denoted  
1223 as  $\Delta S_1$  and  $\Delta S_2$  respectively for the purpose of discussion.  $P$ ,  $Q$  and  $IC$  represent precipitation,  
1224 flow discharge and initial condition, respectively; **e)** The implemented framework in this work  
1225 consisting of ICC and IRC. This figure is adapted from Liao and Barros (2022, 2025b).

1226 **Figure 4** – Map of the Continental United States (CONUS) and headwater basins studied in this  
1227 work. Basin information is available in Table 3. Sub-regions are delineated as the following for  
1228 discussion purposes only: Northern, Central and Southern Appalachian Mountains (NAM, Basin  
1229 21-30; CAM, Basin 13-20; SAM, Basin 01-11). This figure is adapted from Liao and Barros  
1230 (2025b).

1231 **Figure 5** - Examples of raingauge measurements showing the diurnal cycle of different seasons at  
1232 different locations: Left panel – raingauge RG008 located in the eastern ridges for the Summer  
1233 (JAS: July-August-September) season. Right panel – raingauge RG302 located in the western  
1234 ridges for the Spring (AMJ; April-May-June) season. Rain gauge measurements (blue);  
1235 StageIV<sub>DBK</sub> (black); StageIV<sub>DBKC</sub> (green). This figure is from Liao and Barros (2019).

1236 **Figure 6** –Top row – The diurnal cycle of missing precipitation at RG003 (Eastern ridges) and  
1237 RG103 (Inner regions) for January-February-March (JFM) using various products. Bottom row-  
1238 corresponding rain gauge climatology (blue). StageIV<sub>D</sub> (black); StageIV<sub>DBK</sub> (cyan); StageIV<sub>DBKC</sub>  
1239 (green). This figure is from Liao and Barros (2019).

1240 **Figure 7** – Statistical evaluation summary for winter precipitation (JFM, January, February, and  
1241 March): a) Diurnal cycle of mean HSS and TS statistics including all rain gauges calculated using  
1242 all data from 2008 to 2017:  $STIV_D$  (black) and  $STIV_{DBKC}$  (green); b) HSS and TS statistics  
1243 calculated using different rain rate thresholds over the same 10-year period; c) Diurnal cycle of  
1244 rain rate RMSE at seasonal-scale, and its dependence on observed rainfall rate. This figure is from  
1245 Liao and Barros (2019).

1246 **Figure 8** – The IRC-ICC performance in Basin05 as an example for the 2017-10-23 event  
1247 (Basin05: Cataloochee Creek Basin, NC). This event is part of the 2017 Hurricane Nate. This  
1248 figure contains a) hydrological responses when precipitation forcing is the  $STIV_{DBKC}$ . The dashed  
1249 rectangular plot consisting of intermediate results including each iteration from the IRC-ICC  
1250 framework (Figure 3). b) the hydrological equilibrium of the IRC-ICC after 5 iterations. This  
1251 figure is adapted from Liao and Barros (2025b).

1252 **Figure 9** – The IRC-ICC performance for different subregions, include a) 3 events from the  
1253 Southern Appalachians; b) 3 events from the Central Appalachians; and c) 3 events from the  
1254 Northern Appalachians. The IRC-ICC KGE evolution plots from iterations are included below the  
1255 hydrographs. The black and pink line are from the original  $STIV_D$  and the IRC-ICC equilibrium  
1256 state ( $STIV_D^{IRC*}$ ), respectively, and KGE values are displayed as colored numbers in the top left  
1257 corners. This figure is adapted from Liao and Barros (2025b).

1258 **Figure 10** – Event total precipitation maps for three cold season events (a) and three warm season  
1259 events (b). Each column represents one event, and each row represents one precipitation product:  
1260  $STIV_{DBKC}$ ,  $STIV_{DBKC}^{IRC*}$  from IRC-only framework, and  $STIV_{DBKC}^{IRC*}$  from the coupled IRC-ICC  
1261 framework. This figure is adapted from Liao and Barros (2025b).

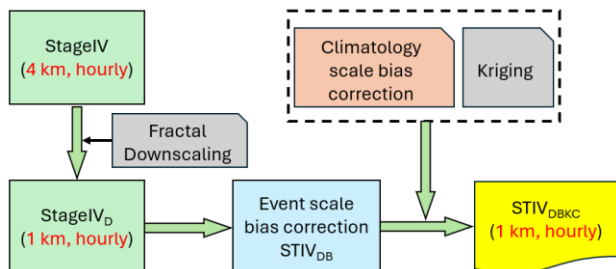
1262 **Figure 11** – Summary charts of precipitation statistics for all event-total precipitation maps. Basin  
1263 precipitation average and standard deviation for each event are represented by circles and triangles  
1264 in the top and bottom panel, respectively. Each panel consists of 3 sub-regions by vertical black  
1265 lines: the Southern Appalachian Mountains, Central Appalachian Mountains, and Northern  
1266 Appalachian Mountains. The list of events in Basin 05 (with event number ranging from 55 to  
1267 108) in the SAM is identified by a blue rectangle for further discussion in the text. The average  
1268 values of all events for both the mean and the standard deviation are calculated and shown in the  
1269 top right corner. Black and pink colors represent pre and post IRC-ICC QPE statistics, respectively.

1270 **Figure 12** – Summary of hydrologic skills. Green dashed lines and associated uncertainty  
1271 envelopes are only for visual illustration. Hydrologic statistics are explained in Table 2. Pink and  
1272 black scatters (each scatter represent one event) represent IRC-ICC, and baseline outputs,  
1273 respectively. Each horizontal panel is split into 3 subsections by vertical black lines representing  
1274 the 3 subregions. Histograms graphs on the right-hand side are provided for a summary view. This  
1275 figure is adapted from Liao and Barros (2025b).

1276 **Figure 13** – a) Event total QPE plots for various QPE datasets conditional on seasons and KGE  
1277 values; b) KGE distributions across events using different QPE datasets. This figure is adapted  
1278 from Liao and Barros (2025b).

1279

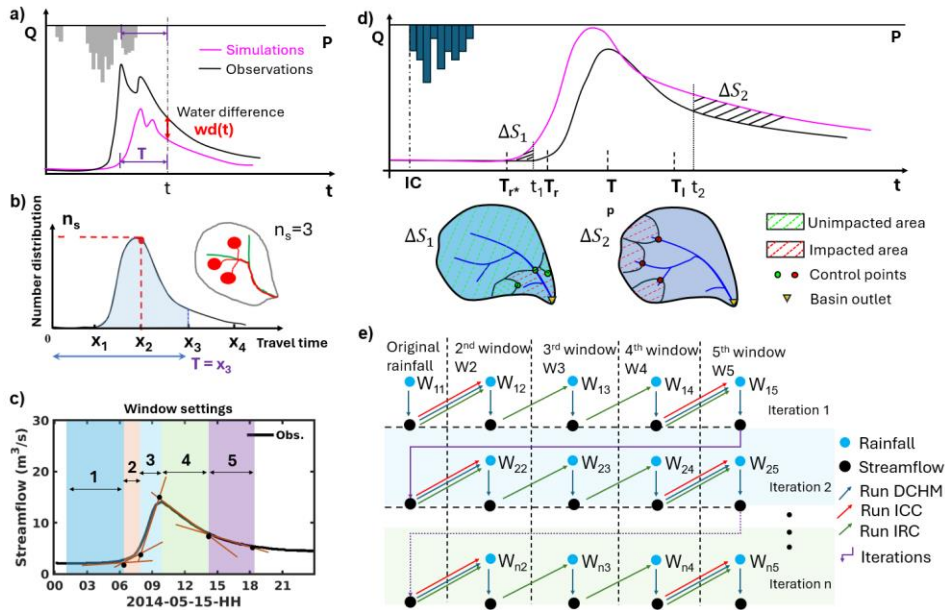




1288

1289 **Figure 2** – Workflow to generate the product STIV<sub>DBKC</sub>.

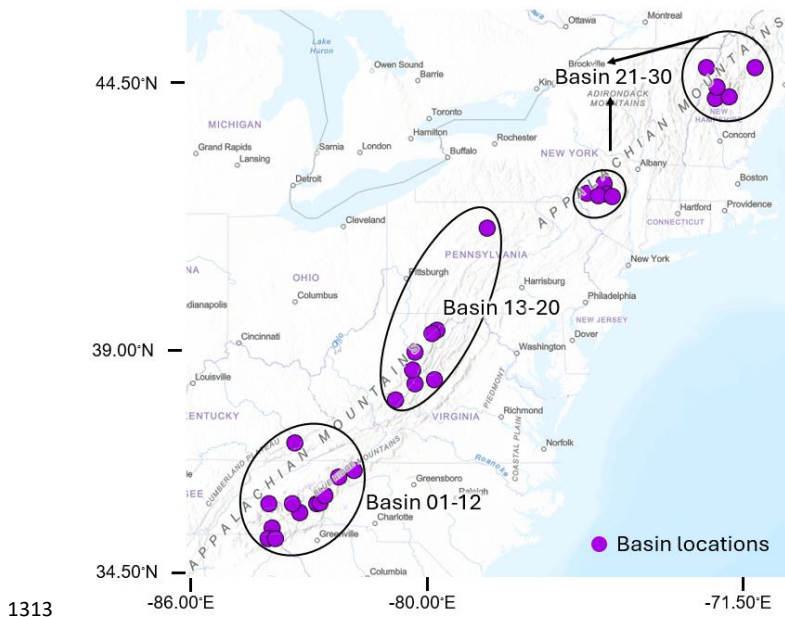
1290



1291

1292 **Figure 3** – An illustration of the structure of IRC, ICC and the coupled IRC-ICC framework  
 1293 including **a)** the residual hydrograph between the observed and simulated discharge, with the  
 1294 discharge water difference  $wd(t)$  being distributed across the time window  $T$ ; **b)** Example of  
 1295 travel time distribution  $TT(t)$  and map (inset) illustrating a hypothetical distribution of runoff  
 1296 source areas (in red,  $n_s=3$ ) with travel time  $x_2$  contributing to streamflow at time  $t$ , meaning  
 1297 that at time  $t-x_2$  there are three pixels ( $n_s=3$ ) generating runoff that reaches the outlet at  
 1298 time  $t$ .  $T$  is the time window over which runoff source areas with  $TT < T$  are mapped and  
 1299 the inverse rainfall correction (IRC) are applied; **c)** Example of IRC windows guided by  
 1300 timescales of dominant hydrological processes. The first window solely covers the initial  
 1301 streamflow conditions before the target event. The second window depicts the early rising  
 1302 limb of the hydrograph. The third window captures the steep rising limb of the hydrograph  
 1303 until it reaches the peak flow. The fourth and fifth windows correspond to interflow-dominant  
 1304 and baseflow-dominant stages of the recession curve respectively, separated by the recession  
 1305 inflection point; **d)** A schematic drawing that shows different characteristic timings in a  
 1306 hydrograph with the implementation of the Initial Condition Correction (ICC) strategy. Specifically,  
 1307  $T_{r^*}$  and  $T_r$  represent the timing of flood front in simulations and observations, respectively.  
 1308  $T_p$  is the timing of observed maximum flood. The inflection point of the recession curve of  
 1309 the observations is denoted as  $T_i$ . Flow differences at  $t_1$  and  $t_2$  are denoted as  $\Delta S_1$  and  
 1310  $\Delta S_2$  respectively for the purpose of discussion.  $P$ ,  $Q$  and  $IC$  represent precipitation,  
 1311 flow discharge and initial condition, respectively; **e)** The implemented framework in this  
 1312 work consisting of ICC and IRC. This figure is adapted from Liao and Barros (2022, 2025b).

1312



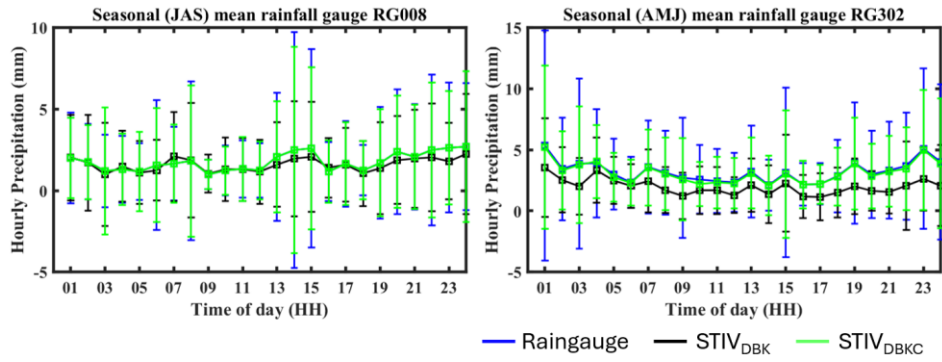
1313

1314 **Figure 4** – Map of the Continental United States (CONUS) and headwater basins studied in this  
 1315 work. Basin information is available in Table 3. Sub-regions are delineated as the following for  
 1316 discussion purposes only: Northern, Central and Southern Appalachian Mountains (NAM, Basin  
 1317 21-30; CAM, Basin 13-20; SAM, Basin 01-11). This figure is adapted from Liao and Barros  
 1318 (2025b).

1319

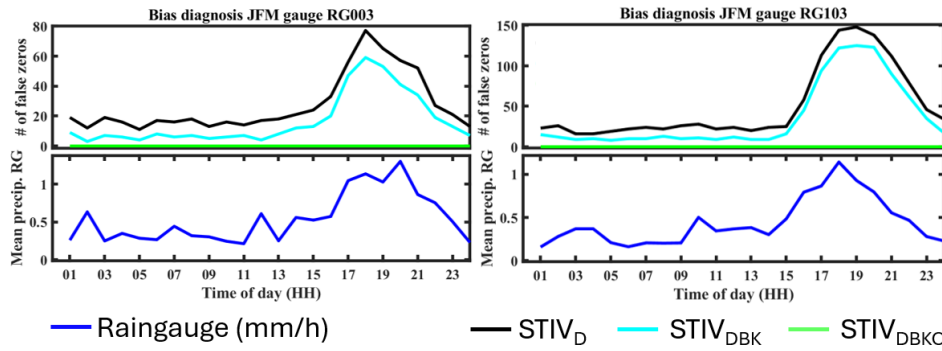
1320

1321



1322 **Figure 5** – Examples of raingauge measurements showing the diurnal cycle of different seasons  
1323 at separate locations: Left panel – raingauge RG008 located in the eastern ridges for the Summer  
1324 (JAS: July-August-September) season. Right panel – raingauge RG302 located in the western  
1325 ridges for the Spring (AMJ; April-May-June) season. Rain gauge measurements (blue);  
1326 StageIV<sub>DBK</sub> (black); StageIV<sub>DBKc</sub> (green). This figure is from Liao and Barros (2019).

1327

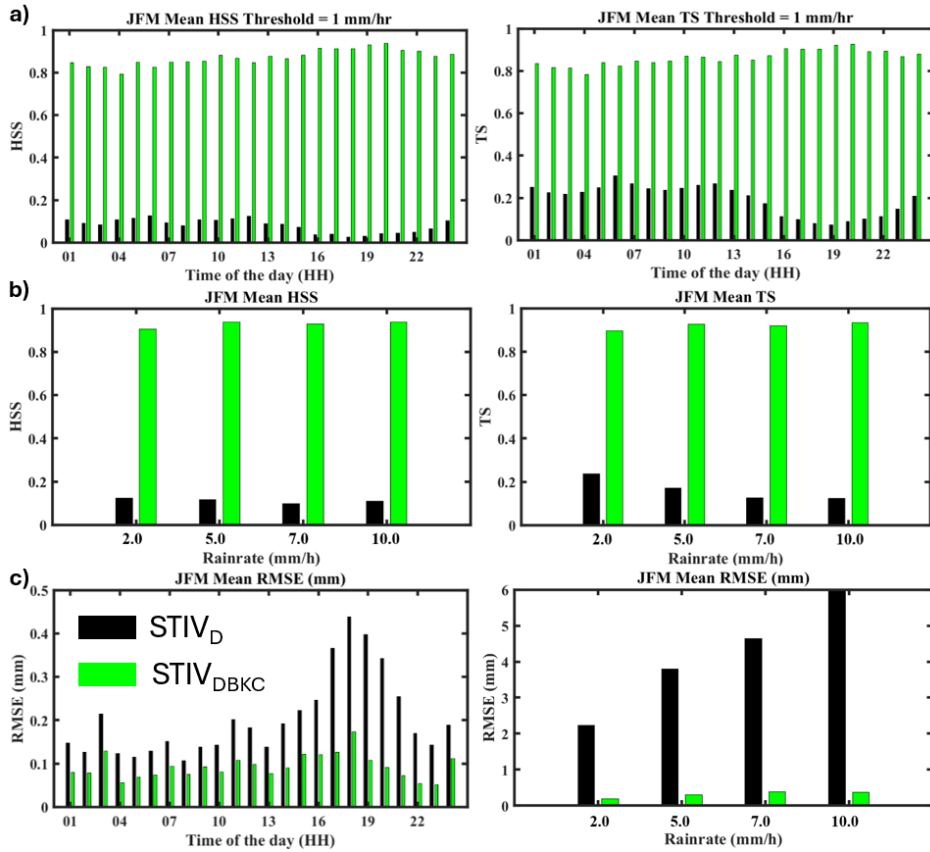


1328

1329 **Figure 6** –Top row – The diurnal cycle of missing precipitation at RG003 (Eastern ridges) and  
 1330 RG103 (Inner regions) for January-February-March (JFM) using various products. Bottom row-  
 1331 corresponding rain gauge climatology (blue). StageIV<sub>D</sub> (black); StageIV<sub>DBK</sub> (cyan); StageIV<sub>DBKc</sub>  
 1332 (green). This figure is from Liao and Barros (2019).

1333

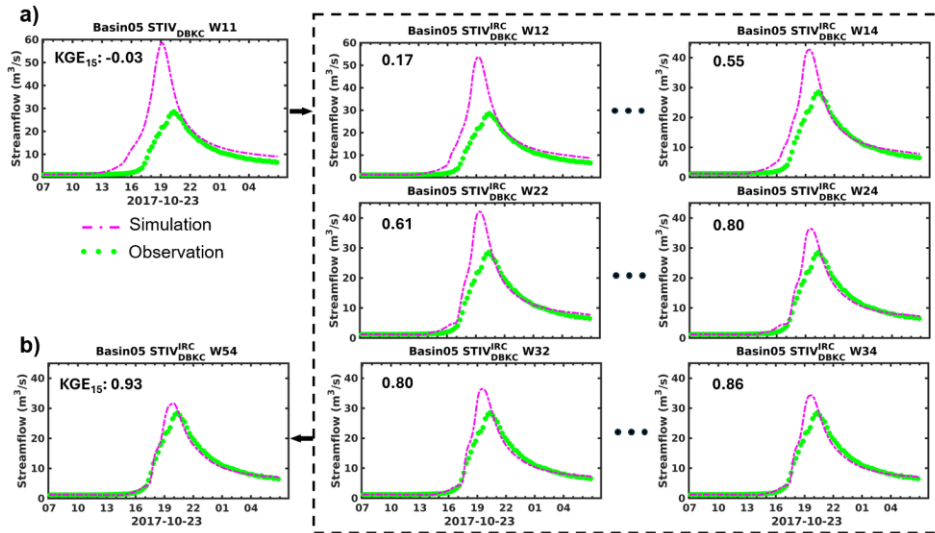
1334



1335

1336 **Figure 7** – Statistical evaluation summary for winter precipitation (JFM, January, February, and  
1337 March): a) Diurnal cycle of mean HSS and TS statistics including all rain gauges calculated using  
1338 all data from 2008 to 2017: STIV<sub>D</sub> (black) and STIV<sub>DBKC</sub> (green); b) HSS and TS statistics  
1339 calculated using different rain rate thresholds over the same 10-year period; c) Diurnal cycle of  
1340 rain rate RMSE at seasonal-scale, and its dependence on observed rainfall rate. This figure is from  
1341 Liao and Barros (2019).

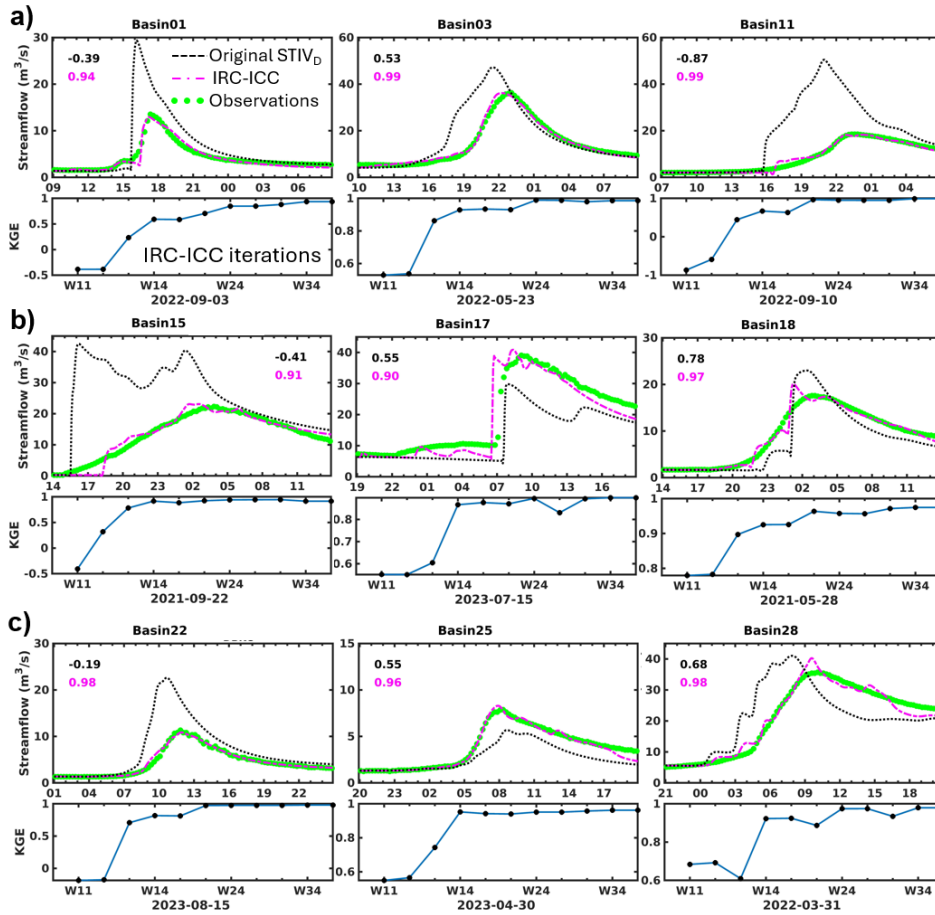
1342



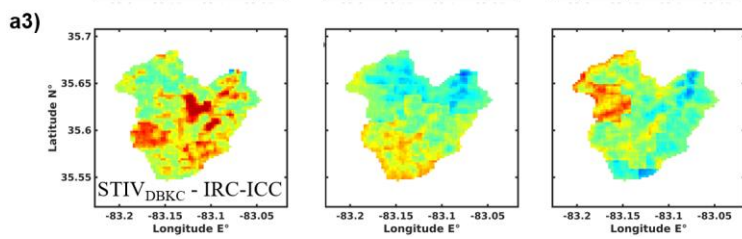
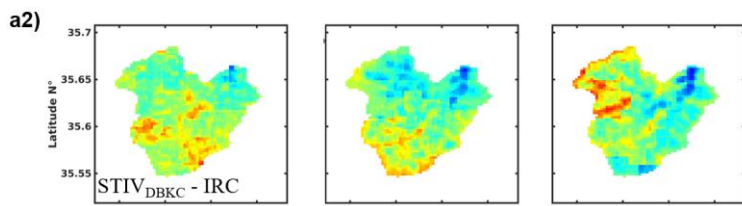
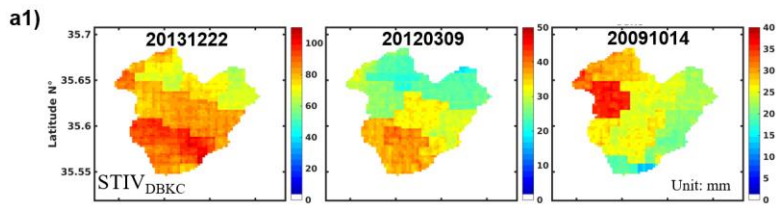
1343

1344 **Figure 8** – The IRC-ICC performance in Basin05 as an example for the 2017-10-23 event  
 1345 (Basin05: Cataloochee Creek Basin, NC). This event is part of the 2017 Hurricane Nate. This  
 1346 figure contains **a)** hydrological responses when precipitation forcing is the  $STIV_{DBKC}$ . The dashed  
 1347 rectangular plot consisting of intermediate results including each iteration from the IRC-ICC  
 1348 framework (Figure 3). **b)** the hydrological equilibrium of the IRC-ICC after 5 iterations. This  
 1349 figure is adapted from Liao and Barros (2025b).

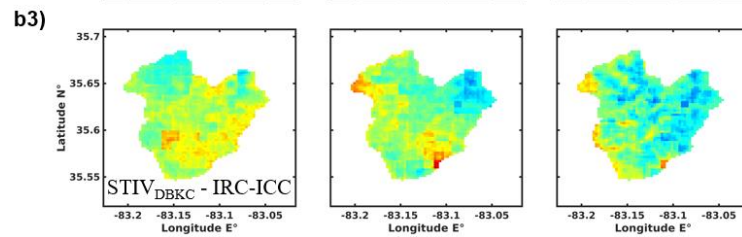
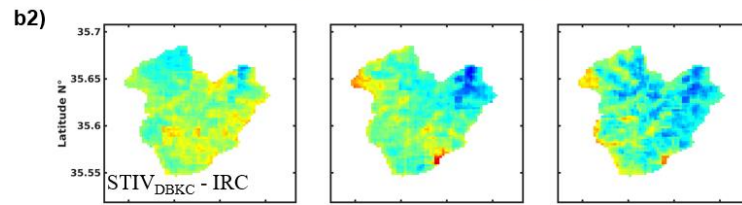
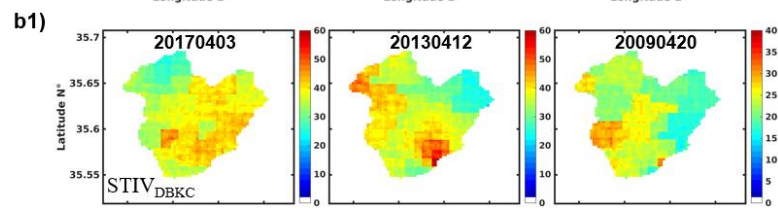
1350



1353 **Figure 9** – The IRC-ICC performance for different subregions, include **a)** 3 events from the  
 1354 Southern Appalachians; **b)** 3 events from the Central Appalachians; and **c)** 3 events from the  
 1355 Northern Appalachians. The IRC-ICC KGE evolution plots from iterations are included below the  
 1356 hydrographs. The black and pink line are from the original  $STIV_D$  and the IRC-ICC equilibrium  
 1357 state ( $STIV_D^{IRC^*}$ ), respectively, and KGE values are displayed as colored numbers in the top left  
 1358 corners. This figure is adapted from Liao and Barros (2025b).



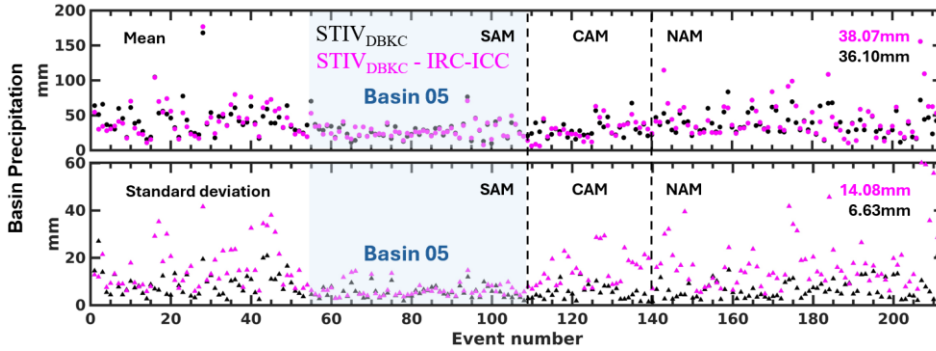
1360



1361

1362  
1363 **Figure 10** – Event total precipitation maps for three cold season events (**a**) and three warm season  
1364 events (**b**). Each column represents one event, and each row represents one precipitation product:  
1365  $STIV_{DBKC}$ ,  $STIV_{DBKC}^{IRC^*}$  from IRC-only framework, and  $STIV_{DBKC}^{IRC^*}$  from the coupled IRC-ICC  
1366 framework. This figure is adapted from Liao and Barros (2025b).  
1367

1368

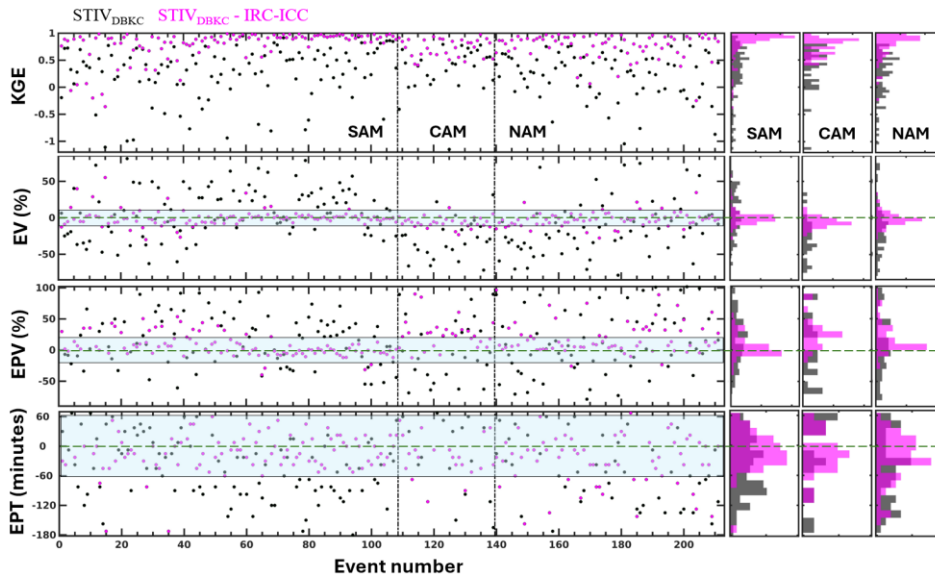


1369

1370 **Figure 11** – Summary charts of precipitation statistics for all event-total precipitation maps. Basin  
1371 precipitation average and standard deviation for each event are represented by circles and triangles  
1372 in the top and bottom panel, respectively. Each panel consists of 3 sub-regions by vertical black  
1373 lines: the Southern Appalachian Mountains, Central Appalachian Mountains, and Northern  
1374 Appalachian Mountains. The list of events in Basin 05 (with event number ranging from 55 to  
1375 108) in the SAM is highlighted by a blue rectangle for further discussion in the text. The average  
1376 values of all events for both the mean and the standard deviation are calculated and shown in the  
1377 top right corner. Black color and pink color represent pre and post IRC-ICC QPE statistics,  
1378 respectively.

1379

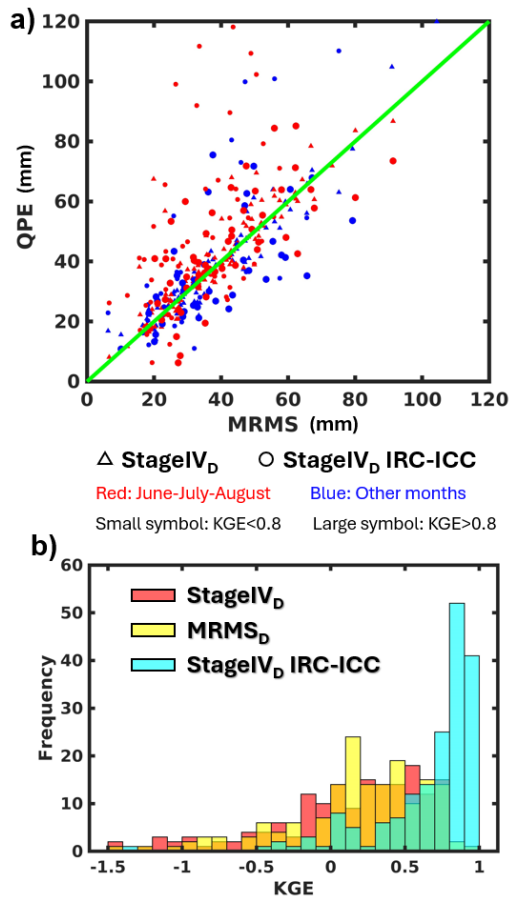
1380



1381

1382 **Figure 12** – Summary of hydrologic skills. Green dashed lines and associated uncertainty  
1383 envelopes are only for visual illustration. Hydrologic statistics are explained in Table 2. Pink and  
1384 black scatters (each scatter represent one event) represent IRC-ICC, and baseline outputs,  
1385 respectively. Each horizontal panel is split into 3 subsections by vertical black lines representing  
1386 the 3 subregions. Histograms graphs on the right hand side are provided for a summary view. This  
1387 figure is adapted from Liao and Barros (2025b).

1388



1389

1390 **Figure 13** – a) Event total QPE plots for various QPE datasets conditional on seasons and KGE  
 1391 values; b) KGE distributions across events using different QPE datasets. This figure is adapted  
 1392 from Liao and Barros (2025b).

1393